Nonlinear Free Vibration Optimization of 2D Tri-axial Braided Composite Fan Blade via ANN, Analytical, FEM, and GA Combined Approach

Mortaza Salehian[1], Hamid Reza Ovesy[*2], Hadi Dabiryan[3]

[1] Department of Aerospace Engineering, Amirkabir University of Technology, Tehran, Iran
[*2] Department of Aerospace Engineering, Amirkabir University of Technology, Tehran, Iran
(Corresponding author, E-mail: ovesy@aut.ac.ir)
[3] Department of Textile Engineering, Amirkabir University of Technology, Tehran, Iran

Abstract

This research aims to enhance the hardening behavior of a non-rotating 2D tri-axial braided composite (2DTBC) fan blade, through investigating the backbone curve characteristics. This enhancement raises the blade's natural frequencies at large oscillation amplitudes, thereby delaying the onset of resonance. A combination of different methods has been employed, including an Artificial Neural Network (ANN), an analytical method, the finite element method (FEM), and a single-objective genetic algorithm (GA). The ANN was used to establish the relationship between the braiding machine parameters and the structural characteristics of the braided fabric. Micromechanical modeling was utilized to determine the mechanical properties of the braided composite. Based on the first-order shear deformation theory (FSDT), the nonlinear free vibration partial differential equations of the composite blade shell were derived using Hamilton's principle. The FEM was employed to solve the differential equations and obtain the corresponding backbone curves. Finally, a single-objective genetic algorithm was deployed to optimize the braided composite structure in order to increase the hardening behavior of the blade. The obtained results demonstrate the viability of the proposed approach. The results indicate that the hardening behavior has increased by a factor of 6.8 compared to the non-optimized case.

Keywords. Tri-axial braided; braiding angle and space; artificial neural network; nonlinear vibration; backbone curve

1- Introduction

Blades are critical components in turbine and propulsion systems, such as gas turbines, wind turbines, turbofan engines, turbojet engines and turboprop engines, which operate under harsh temperature, pressure, and dynamic load conditions. Enhancing their durability and performance is crucial, leading to the investigation of advanced materials and complex modeling techniques [1-3].

Traditional metal materials are increasingly being replaced by composites and nano-reinforced composites, such as those incorporating graphene platelets (GPLs) and carbon nanotubes (CNTs) [1, 3, 4]. These materials are highly effective in enhancing mechanical properties and decreasing weight, providing a greater thrust-weight ratio for applications like aero-engines [2-4]. Functionally Graded Materials (FGMs), where the variation of material properties is continuous through the thickness, are also suggested to reduce inter-laminar stresses and prevent abrupt damage, addressing challenges like the spalling of ceramic layers in thermal and environmental barrier coatings (TEBCs) [1]. Functionally graded graphene platelet (FGGP) reinforced composites are specifically noted for their potential in manufacturing blades with better mechanical properties and lighter weights [4]. Dispersing graphene platelets layer-wise into materials like polymer matrix or titanium alloy can enhance mechanical performance, with studies indicating that increasing the concentration of GPLs near the top and bottom surfaces yields the highest efficiency in improving structural dynamics [5]. The nonlinear vibration of rectangular plates has been examined in recent studies, with the effects of geometric nonlinearity, and boundary conditions being highlighted, and nanocomposites, laminated composites, and metallic plates analyzed through advanced numerical and experimental approaches. The role of natural boundary conditions and nonlinear damping has also been clarified in accurately predicting large-amplitude dynamic responses [6-8].

Specific objectives of some studies include investigations into the free oscillation of thin-walled composite beams, where non-classical effects like constrained warping and transverse shear are considered important, and the assumptions made in constitutive equations significantly influence natural frequencies [9], studying the dynamic characteristics of dual-rotor systems with bearing defects

and aerodynamic excitation [10]. Research also focuses on the free vibration behavior of rotating beams composed of FGMs, comparing different beam theories and incorporating material property uncertainties [11]. Additionally, the dynamic characteristics and vibration resonance of braided composite gear transmission systems are analyzed, with findings suggesting that lightweight composite designs can enhance system stability [12]. For non-composite structures, studies examine the free and viscoelastic unforced vibration of nanoscaled beams and plates using nonlocal integral -based elasticity, showing that parameters like nonlocal effects and viscoelasticity influence natural frequencies [13-15]. The dynamic response of blade disk rotor systems is also investigated, particularly focusing on how factors like structural cracks and aerodynamic loading introduce specific frequency components into the vibration response [16].

Rotating blades operate in a complex environment, involving aerodynamic, elastic, and inertia forces, which may cause large-amplitude nonlinear vibrations. [2, 17]. High rotating speeds introduce significant centrifugal forces and Coriolis effects [2, 18]. The blade's complex configuration, often curved and twisted with varying cross-sections and thickness, necessitates advanced modeling approaches [5, 17, 19-22]. While simplified models like beams have been used, shell models are considered more suitable and accurate for describing the dynamics of curved and twisted blades [19, 23]. Various theories are employed for modeling, including classical plate theory, FSDT, higher-order shear deformation theories, and nonlinear shell theories like von Kármán and Novozhilov nonlinear shell theory [3, 17, 19, 20, 22-26]. These theories are often combined with geometric nonlinearity assumptions to capture significant amplitude vibrations [1, 3, 5, 17, 19, 20, 22, 23, 27-29].

Numerous studies investigate the nonlinear dynamic response of composite and functionally graded blades under various conditions. Some studies focus on dynamic responses under varying rotating speeds [2, 17, 18, 30]. Centrifugal load in conjunction with material anisotropy and pre-twist can induce static torque [24]. Geometric features such as pre-twist, presetting angles, variable cross-sections, and thickness variations are studied for their influence on vibration characteristics and nonlinear behavior [3, 20-25, 27, 31]. The pre-twisted shape significantly affects vibration characteristics [24]. Regarding

external loading, blades are subjected to various external forces, including aerodynamic loads (transverse and axial) and blade-casing rubbing [2, 17, 19, 25, 32-34]. Some studies propose novel dynamic models for axial excitation considering aerodynamic load in the tip gap and rubbing [4, 19, 32, 34]. Leakage flows at the tip gap are also considered a source of axial excitation [4, 19, 34]. Subsonic airflow is often considered a transverse excitation, sometimes derived using the Vortex Lattice Method (VLM) [19, 24, 25, 32]. The temperature rise also play a critical role in composite and FG blades' vibration characteristics and nonlinear dynamics [2, 3, 19, 31, 35]. Material properties that vary with temperature and are graded through the thickness are considered. High temperatures can strengthen the nonlinear softening behavior of blades with thermal barrier coatings [35]. Material properties are another significant focus. Studies analyze the effects of graphene distribution patterns, weight fractions, matrix cracks, and material property variation on vibration frequencies and nonlinear responses [4, 19, 20, 23, 27]. Lastly, the effect of initial geometric imperfection on the free vibration characteristics and dynamic stability has also been explored [4, 19, 33].

The study of nonlinear vibrations is crucial because it reveals complex dynamic behaviors beyond linear predictions, including super-harmonic, sub-harmonic, and primary resonances [2]. Some researches investigate various types of resonance, such as primary resonance [2, 4, 19, 21, 32-35] and internal resonance [17, 19, 21, 24, 25, 32, 35]. Phenomena like saturation and jumping between vibration modes are also observed under subsonic airflow excitation [24, 25].

Furthermore, the nonlinear dynamics of blades exhibit complex behaviors, including bifurcation [2, 4, 17, 25, 32-34] and chaotic dynamics [2, 4, 17, 19, 21, 25, 32-34]. These complex behaviors, including almost-periodic responses, typical period-doubling and anti-period-doubling bifurcation vibrations, and hyperchaos, highlight the richness of the nonlinear dynamics of aero-engine blades [2, 33]. Engineers must study these dynamics to understand blade behavior comprehensively and ensure aircraft safety, as resonances and complex dynamics can accelerate blade damage [2].

Various numerical methods are utilized to solve the governing equations, including the FEM [1, 22, 23, 30], Rayleigh-Ritz method [5, 19-21, 24, 36], Galerkin method [17, 19, 33], Method of Multiple Scales

[19, 21, 25, 32], Runge-Kutta method [4, 33, 34], Chebyshev polynomials [29, 30, 37], and element-free methods like the Improved Moving Least-Square Ritz (IMLS-Ritz) method, which offer advantages for complex geometries and large deformations [3, 27, 29, 31]. Comparison studies with experimental data and other numerical methods are often conducted to validate the accuracy and efficiency of the proposed models [4, 5, 20, 22, 24, 27, 30, 33, 34].

Vibration optimization of rotating blades and similar structures is an important issue. A primary goal of such efforts is often to improve structural vibration characteristics [18, 20, 34, 38]. This can involve preventing structural resonance [23, 38], a crucial factor for reliable blade design, given that fatigue resulting from extreme vibrations is the primary cause of failure. [21]. Optimization may aim to maximize natural frequencies and damping ratios [28, 39]. Another objective can be to optimize vibration amplitude and trajectory [30]. The sources highlight that understanding the dynamic behavior of rotating blades holds significant engineering value for optimizing their geometric design [38]. Reasonable modeling and dynamic analysis provide valuable insights for optimizing rotating blades [20, 38].

Optimization approaches include an isogeometric shape optimization technique where control point coordinates are used as design parameters for variable-section blades to find an optimal lightweight shape while avoiding resonance [38]. Structural optimization using methods like finite element analysis and genetic algorithms has been performed on rotating tapered laminated plates to maximize natural frequencies and damping characteristics [28]. Lay-up configuration of rotating cross-ply laminated nanocomposite blades has also been investigated for optimization [34]. Additionally, parametric studies analyzing the effects of various parameters like material distribution (e.g., graphene platelet distribution [3, 20, 29], functional grading [20, 24]), geometric features (e.g., taper ratios [24, 28], variable thickness [31, 38], pre-twist angle [3, 24, 29]), and operational conditions (e.g., rotation speed [3, 24, 29]) on vibration characteristics contribute fundamental knowledge for optimization [3, 20, 24, 29, 31]. Tailoring studies using specific structural models have shown to enhance natural frequency characteristics [18]. Advanced materials like functionally graded materials and nanocomposites (e.g.,

reinforced with graphene platelets or carbon nanotubes) are explored for their potential to improve properties and shape dynamic behavior [23, 24]. Some studies have also explored using a harmonic balance method combined with sensitivity analysis as a design optimization strategy for accommodating mechanical systems to optimize vibration amplitude and trajectory [30].

The ANNs have been utilized in analyses related to the dynamics and design of structures like helicopter rotor blades [40]. Specifically, a Back Propagation (BP) Neural Network is a widely used model [41-46] and was developed as a fast predictive model to estimate the nonlinear response and aerodynamic characteristics of an Active Control Flap (ACF) for applications like vibration and noise reduction [40]. This network showed high prediction accuracy and reliability after training [40]. Additionally, artificial neural networks have been part of knowledge-based methods for designing heterogeneous turbine blades, suggesting their use in analyzing blade properties influenced by vibrations [40].

In a previous study [39], the authors attempted to increase the linear natural frequencies of a non-rotating 2D tri-axial braided composite (2DTBC) fan blade through an eigen-value analysis. The current research aims to enhance the hardening behavior of the blade by optimizing the structural parameters of a 2DTBC. Given that a fan blade is subjected to severe loading conditions, it experiences large deformations, necessitating the investigation of nonlinear vibrations for a realistic analysis. In such cases, the natural frequency changes with increasing deformation amplitude, a phenomenon illustrated by the backbone curve. Ideally, the natural frequency should increase with larger deformation amplitudes, which is referred to as a hardening backbone curve. This study aims to maximize the hardening behavior. This study employs an ANN to establish the relationship between braiding machine parameters and the braided structure. Micromechanics is used to determine the mechanical properties of the 2DTBC. Hamilton's principle is applied to derive the differential equations of the composite blade shell, and the finite element method is used to solve these equations and calculate the backbone curve. Finally, a single-objective genetic algorithm is implemented to increase the hardening behavior. Notably, prior studies have largely addressed linear and nonlinear vibrations of beams, plates, and shells. In particular, the previous closely related work has investigated the optimization of linear

dynamic properties of a 2DTBC blade. However, an integrated optimization of nonlinear dynamic performance—specifically the hardening behavior—of 2DTBC blade structures has not been previously reported. The literature reviews explicitly states that existing studies do not consider a process–structure–property–performance framework in which manufacturing parameters are systematically linked to structural configuration, material properties, and nonlinear dynamic response. The present study is the first to employ an integrated framework that combines an ANN, analytical method, FEM, and a GA to optimize the nonlinear hardening behavior of a 2DTBC blade. Also, due to its unique structure, 2DTBCs offer greater optimization potential than conventional composites.

2- Framework construction

Similar to the earlier study [39], a combined framework construction incorporating an ANN, an analytical method, the FEM, and a GA optimization was employed. This framework construction is schematically illustrated in Fig. 1.

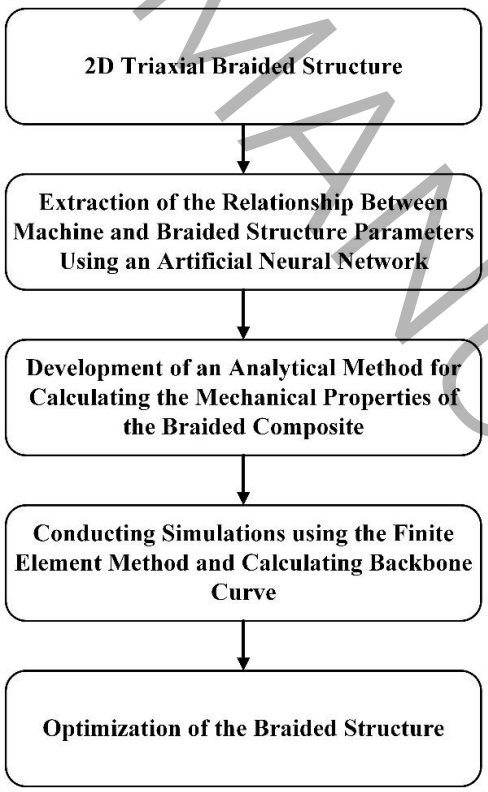

Fig. 1 Overview diagram of the entire research process

2-1- Experimental design method

The Response Surface Methodology (RSM) was utilized to explore how the braiding machine's independent parameters influence the resulting braided structure. The RSM is an empirical model that uses mathematical and statistical techniques to relate input variables to responses. This approach allows for efficient analysis by examining a strategically selected subset of input parameter combinations rather than testing all possible variations. This not only ensures reliable results but also reduces time and resource consumption.

The key independent parameters considered in the braiding process were carrier speed (V_c), take-off speed (V_t), chord length (c) and yarn count (D). The fabrication of braided shell samples is constrained by the capabilities of the braiding machine. The parameters are each restricted to specific upper and lower bounds, and all experiments must comply with these permissible ranges. Table 1 outlines the specific ranges for each of these parameters.

Table 1. Parameter analysis for response surface method.

Parameter	Code	Unit	Level				
Take-off speed	V_t	m/min	0.143	0.213	0.301	0.410	0.542
Carrier speed	V_c	rpm	5.666	6.376	7.086	-	-
Chord length	c	cm	3	4.5	6	-	-
Yarn count	D	tex	400	800	1200	-	-

Using RSM, 15 distinct parameter combinations were generated, as presented in Table 5 of previous work [39]. These combinations were experimentally applied to produce braided structures on three-blade samples with airfoil-shaped cross-sections and chord lengths of 3, 4.5, and 6 cm using the braiding machine. Following fabrication, the structure parameters of the braided samples specifically the braiding angle and braiding space were evaluated using image processing techniques. Four selected example images for image processing of the braided structure parameters are prominently shown in Fig. 2. The measured results are compiled in Table 7 of previous work [39].

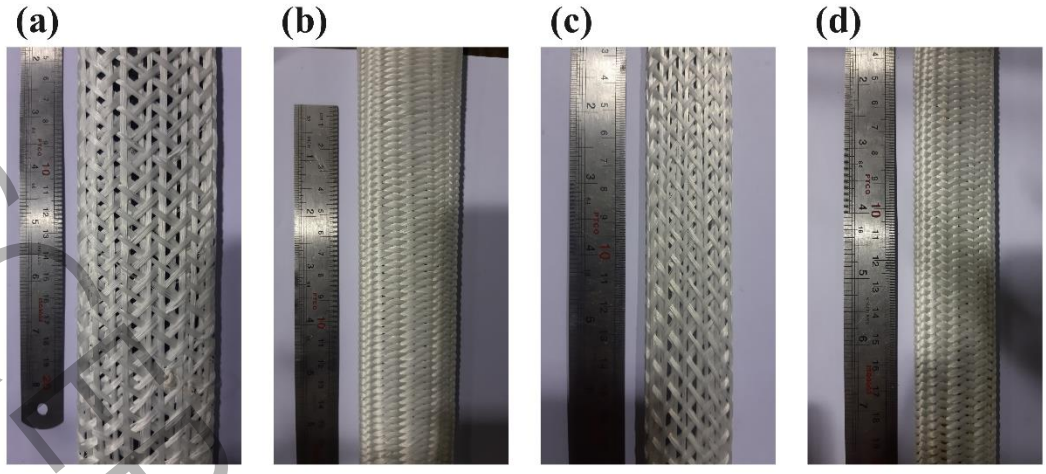

Fig. 2 Image processing; (a) sample 1, (b) sample 9, (c) sample 11, and (d) sample 14

2-2- ANN-based simulation

We employed an ANN to establish the relationship between the braided structure parameters and the independent parameters of the braiding machine. The independent parameters of the braiding machine include carrier speed, take-off speed, chord length, and yarn count, while the braided structure parameters are braiding angle and space. Fig. 2 from [39] includes a Pearson correlation heat map to evaluate the relationships between input parameters, the reliability of the model's generalization capability through a 5-fold cross-validation method, and modeling the relationship between the braiding machine parameters and the braided structure by a feedforward backpropagation neural network in MATLAB. Two distinct networks, each with a single output, were employed to optimize prediction performance. The architecture of these two separate networks utilized tangent sigmoid transfer functions for the hidden layers and a purely linear function for the output layers. Grid search (5 to 10 nodes) was used to optimize the number of nodes in the hidden layer. The adjustment of key parameters such as learning speed (0.1), momentum amount (0.9), and training epochs (1000) was performed utilizing the Levenberg-Marquardt (LM) learning procedure. The LM procedure increases the training of feedforward backpropagation neural networks by mixing specifications of gradient descent and Newton approaches. This method facilitates optimization fast convergence and high precision, especially when dealing with complex and demanding problems. By automatically adjusting between

these two approaches, the LM procedure decreases the likelihood of getting trapped in local minima and is suitable for small to medium-sized networks.

To evaluate model performance and generalization, a novel composite performance index, referred to as the Total Goodness Function (TGF), was adopted. This metric has been introduced and validated in our previous works and has demonstrated high sensitivity and robustness across multiple engineering prediction problems. Unlike single metrics, TGF simultaneously accounts for both goodness-of-fit and prediction error in training and testing phases. The Total Goodness Function is defined as:

$$TGF = \frac{1}{N}\sum_{1}^{2} n_i \left(R_i^2 + e^{-MSE_i}\right) \tag{1}$$

Where N is the total number of data points $(N=15)$, n_i denotes the number of samples associated with the training or testing subset, R_i^2 is the coefficient of determination, and MSE_i is the mean squared error for each subset. The theoretical upper bound of TGF is 2, corresponding to perfect predictive performance. During model development, optimization was directed toward maximizing TGF and driving it as close as possible to this ideal value. Fig. 3 presents the results of the sensitivity analysis, which was conducted, revealing the impact of each input variable. The Fig. 3 also illustrates the extent of each independent braiding machine parameter's influence on the braided structure parameters.

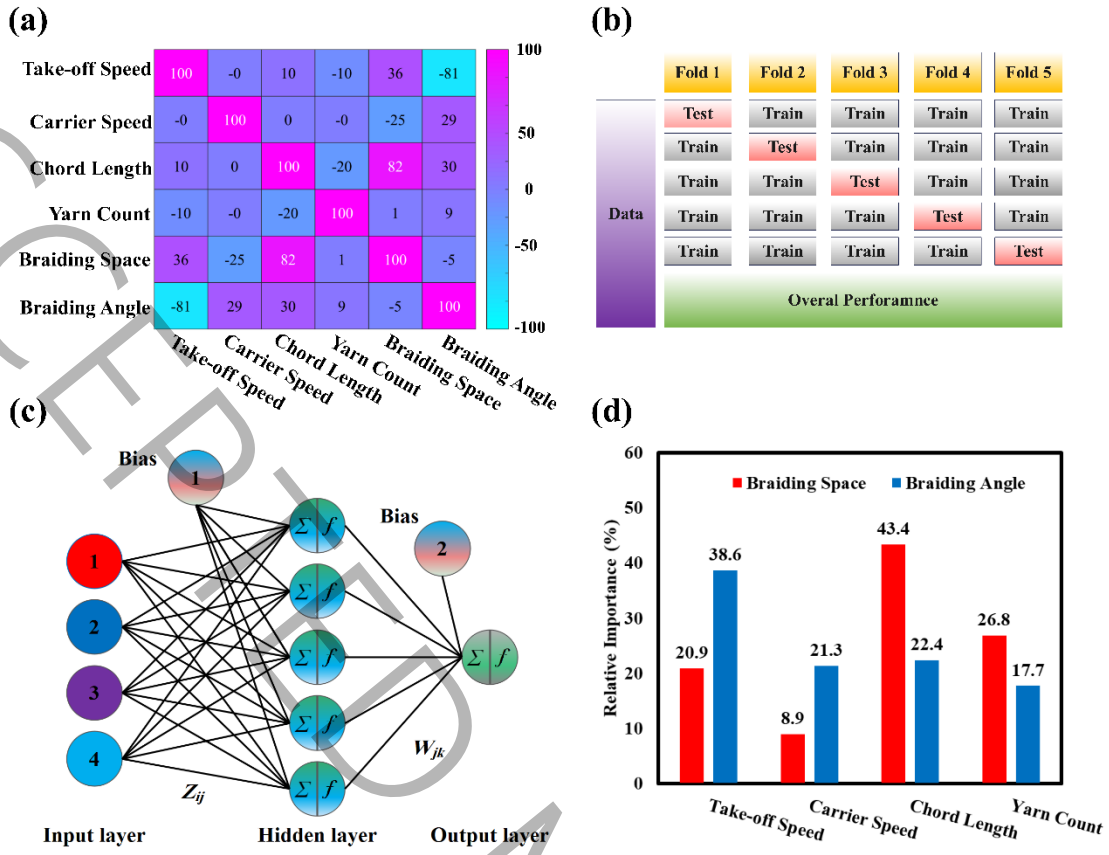

Fig. 3 Representation of the artificial neural network modeling architecture; (a) Pearson's correlation heatmap matrix of experimental data, (b) schematic presentation of 5-fold cross-validation, (c) topology of developed neural network, (d) relative importance of input parameters of Fold 1 [39]

Table 2 and Table 3 present the trainable parameters of the neural network, corresponding to the braiding space and angle variables, respectively.

Table 2. Weight and bias values of network developed for braiding space.

	Weight						Bias
	-0.9766	-0.0101	1.9892	0.9210			2.4880
	2.9852	-0.5555	1.9907	2.6829			-0.8990
Z	-0.6009	0.5525	-2.4825	-0.4685		1	-1.1481
	-0.4678	-0.8603	2.1195	2.4317			-1.7546
	-1.3458	-0.2564	1.0246	-2.0006			-2.2218
W	-0.3923	0.3158	-0.6136	0.3540	0.2251	2	0.4074

Table 3. Weight and bias values of network developed for braiding angle.

	Weight						Bias
	1.6435	-0.5931	-2.6452	-0.9658			-1.6593
	-0.6623	-2.0931	1.0760	0.3572			1.2155
Z	0.3956	-0.2924	-0.2517	-2.1813		1	-0.0711
	-0.8766	1.7182	0.2418	1.3586			-1.6146
	4.0820	1.0354	-0.4182	-0.3301			1.4925
W	-0.5219	-0.2486	0.1498	0.1264	-0.5595	2	0.0040

2-3- Equivalent mechanical properties of the 2DTBC

A tri-axial braided structure is formed from three main yarns: two diagonally interlaced yarns, known as bias yarns, and a third, called the axial yarn, which runs along the bisector between the two bias directions, threading through them. Micromechanical theory is utilized to evaluate the mechanical behavior of such composites. The theory is a method that analyzes composite materials at the level of their constituent components and their interactions. This process begins with defining a unit cell at the micro-scale, where each yarn, saturated with resin, is treated as a unidirectional composite, and its properties are estimated using the Chamis' equations [39]. Then, a representative volume element (RVE) is selected at the mesoscale according to Fig. 4 [39].

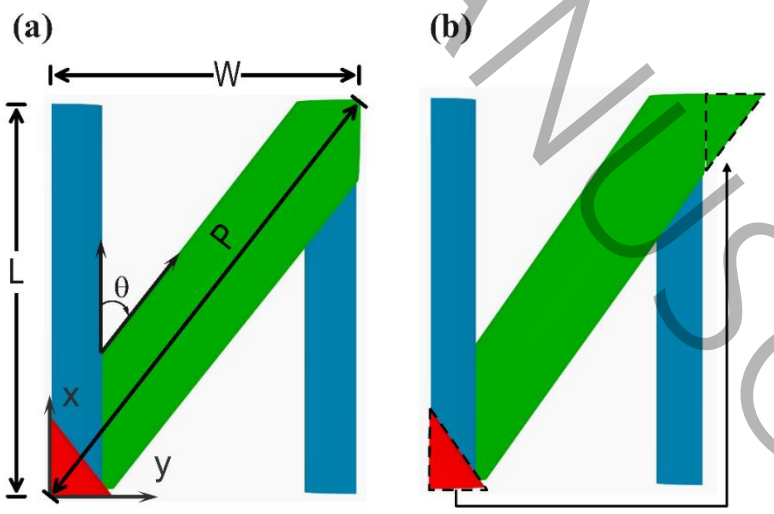

Fig. 4 Representation of RVE architecture; (a) a mesoscale RVE model, (b) transferring of bias fiber tow [39]

Fig. 5 illustrates the trajectory of the bias yarn and the cross-section of the axial yarn. As can be observed, the path of the bias yarn follows a cosine-shaped trajectory, and at each point this path forms an angle with the horizontal plane, which is referred to as the undulation angle [39].

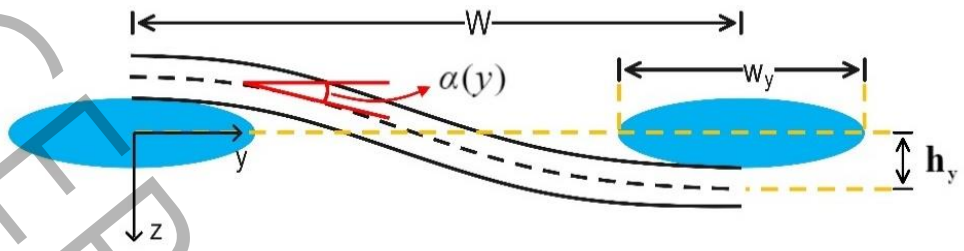

Fig. 5 Undulation profile of the unit cell [39]

h_y represents the yarn thickness, and w_y denotes the yarn width. Therefore, in the yz plane, the equation of the bias yarn trajectory can be expressed as follows [39].

$$z = -h_y \cdot \cos\left(\frac{y}{w_y} \cdot \pi\right) \tag{2}$$

The equivalent stiffness matrix of the bias yarn, considering both the undulation and braiding angle, is calculated by averaging the local stiffness matrices as follows [39].

$$\sigma_b = \int_0^W R^T \cdot \left[C^{local}\right] \cdot R \cdot \frac{dy}{\cos(\theta)} \cdot \varepsilon_b = \left[C_b^{eq}\right] \cdot \varepsilon_b \tag{3}$$

Finally, the equivalent stiffness matrix of the entire braided composite is obtained using the volumetric averaging method [39, 47].

$$C^{global} = \frac{V_b \cdot C_b^{eq} + V_a \cdot C_a^{eq} + V_m \cdot C_m^{eq}}{W \cdot L \cdot H} \tag{4}$$

a is the axial yarn symbol, b is the bias yarn symbol, m is the matrix symbol, w is the composite width, H is the composite thickness, L is the composite length, V is the volume symbol, and C is the stiffness symbol. Glass fibers and epoxy resin were used to fabricate the 2DTBC. These two materials' mechanical and physical properties are provided in Table 4, [39].

Table 4 Elastic properties of glass fibers and epoxy resin, [39]

Property	Fiber	Matrix
Material type	E-Glass	Epoxy LR625
Elastic modulus (GPa)	73.98	2.79
Shear modulus (GPa)	29.92	1.03
Poisson's ratio	0.22	0.35
Density (g/cm^3)	2.54	1.16

2-4- Governing differential equations for composite shells

The FSDT is employed for the displacement field, and the strain field is considered based on the von Karman nonlinear strains for thin shallow shells as follows [48]. The assumptions considered for the shells are summarized as follows:

- The layers are perfectly bonded together.
- Each layer is of uniform thickness.
- Normals to the shell reference surface are assumed to be inextensible in the transverse direction.
- The normal vector to the shell reference surface remains straight after deformation, but is not necessarily perpendicular to the deformed surface.
- Shell strains are small and the displacements are large, and the corresponding response is treated as nonlinear.

$$\begin{aligned}
&\varepsilon_1 = \left(\varepsilon_1^0 + \zeta \cdot \varepsilon_1^1\right)\\
&\varepsilon_2 = \left(\varepsilon_2^0 + \zeta \cdot \varepsilon_2^1\right)\\
&\varepsilon_4 = \varepsilon_4^0\\
&\varepsilon_5 = \varepsilon_5^0\\
&\varepsilon_6 = \left(\varepsilon_6^0 + \zeta \cdot \varepsilon_6^1\right) = \left(\omega_1^0 + \omega_2^0\right) + \zeta \cdot \left(\omega_1^1 + \omega_2^1\right)
\end{aligned} \tag{5}$$

Where

$$\varepsilon_1^0 = \frac{1}{a_1} \cdot \left(u_{0,1} + \frac{1}{a_2} \cdot a_{1,2} \cdot v_0 + \frac{a_1}{R_1} \cdot w_0 + \frac{1}{2 \cdot a_1} \cdot {w_{0,1}}^2 \right) \tag{6}$$

$$\varepsilon_2^0 = \frac{1}{a_2}\cdot\left(v_{0,2} + \frac{1}{a_1}\cdot a_{2,1}\cdot u_0 + \frac{a_2}{R_2}\cdot w_0 + \frac{1}{2\cdot a_2}\cdot {w_{0,2}}^2\right)$$

$$\varepsilon_4^0 = \frac{1}{a_2}\cdot\left(w_{0,2} + a_2\cdot\phi_2 - \frac{a_2}{R_2}\cdot v_0\right)$$

$$\varepsilon_5^0 = \frac{1}{a_1}\cdot\left(w_{0,1} + a_1\cdot\phi_1 - \frac{a_1}{R_1}\cdot u_0\right)$$

$$\omega_1^0 = \frac{1}{a_1}\cdot\left(v_{0,1} - \frac{1}{a_2}\cdot a_{1,2}\cdot u_0 + \frac{1}{2\cdot a_2}\cdot w_{0,1}\cdot w_{0,2}\right)$$

$$\omega_2^0 = \frac{1}{a_2}\cdot\left(u_{0,2} - \frac{1}{a_1}\cdot a_{2,1}\cdot v_0 + \frac{1}{2\cdot a_1}\cdot w_{0,1}\cdot w_{0,2}\right)$$

$$\varepsilon_1^1 = \frac{1}{a_1}\cdot\left(\phi_{1,1} + \frac{1}{a_2}\cdot a_{1,2}\cdot\phi_2\right)$$

$$\varepsilon_2^1 = \frac{1}{a_2}\cdot\left(\phi_{2,2} + \frac{1}{a_1}\cdot a_{2,1}\cdot\phi_1\right)$$

$$\omega_1^1 = \frac{1}{a_1}\cdot\left(\phi_{2,1} - \frac{1}{a_2}\cdot a_{1,2}\cdot\phi_1\right)$$

$$\omega_2^1 = \frac{1}{a_2}\cdot\left(\phi_{1,2} - \frac{1}{a_1}\cdot a_{2,1}\cdot\phi_2\right)$$

R_1 and R_2 denote the principal radii of curvature associated with the mid-surface. Additionally a_1, and a_2 denote the Lamé coefficients. For convenience, the spatial and temporal derivatives are denoted as $\partial/\partial\xi_1 = (\ )_{,1}$, $\partial/\partial\xi_2 = (\ )_{,2}$, $\partial/\partial x = (\ )_{,x}$, $\partial/\partial y = (\ )_{,y}$ and $\partial u/\partial t = \dot{u}$ in the subsequent formulations. By calculating the strain energy and kinetic energy of the system and applying Hamilton's principle, the governing differential equations for the blade's behavior are obtained as follows [48]. The principle is a fundamental variational principle in classical mechanics that describes the true path of a dynamical system between two fixed points in configuration space over a given time interval, and presents the action as a stationary function, where the action is defined as the Lagrangian time integral, which is itself a function of kinetic energy and potential energy. Parameters $\left(u_0, v_0, w_0, \phi_x, \phi_y\right)$ represent the degrees of freedom of the model $\left(x_1 = x,\quad x_2 = y\right)$.

$$N_{xx,x}+\left(N_{xy}+C_0\cdot M_{xy}\right)_{,y}+\frac{Q_x}{R_1}=\left(I_0\cdot\ddot{u}_0+I_1\cdot\ddot{\phi}_x\right) \tag{7}$$

$$\left(N_{xy}-C_0\cdot M_{xy}\right)_{,x}+N_{yy,y}+\frac{Q_y}{R_2}=\left(I_0\cdot\ddot{v}_0+I_1\cdot\ddot{\phi}_y\right) \tag{8}$$

$$Q_{x,x}+Q_{y,y}-\left(\frac{N_{xx}}{R_1}+\frac{N_{yy}}{R_2}\right)+\mathbb{N}\left(w_0\right)=I_0\cdot\ddot{w}_0 \tag{9}$$

$$M_{xx,x}+M_{xy,y}-Q_x=\left(I_2\cdot\ddot{\phi}_x+I_1\cdot\ddot{u}_0\right) \tag{10}$$

$$M_{xy,x}+M_{yy,y}-Q_y=\left(I_2\cdot\ddot{\phi}_y+I_1\cdot\ddot{v}_0\right)$$

$$C_0=\frac{1}{2}\cdot\left(\frac{1}{R_1}-\frac{1}{R_2}\right),\quad \frac{1}{\partial x}=\frac{1}{a_1}\cdot\frac{1}{\partial\xi_1},\quad \frac{1}{\partial y}=\frac{1}{a_2}\cdot\frac{1}{\partial\xi_2} \tag{11}$$

The quantities $\left(N_{xx},N_{yy},N_{xy}\right)$ denote the in-plane force resultants and $\left(M_{xx},M_{yy},M_{xy}\right)$ correspond to the bending moment resultants. The terms Q_x and Q_y refer to the transverse shear force resultants, and $\left(I_0,I_1,I_2\right)$ represent the mass moments of inertia.

$$I_0=\int_{-h/2}^{h/2}\rho\cdot z^i\cdot dz,\qquad \left(i=0,1,2\right) \tag{12}$$

Here, ρ denotes the density of the laminated composite material, and

$$\mathbb{N}\left(w_0\right)=\left(N_{xx}\cdot w_{,x}+N_{xy}\cdot w_{,y}\right)_{,x}+\left(N_{xy}\cdot w_{,x}+N_{yy}\cdot w_{,y}\right)_{,y} \tag{13}$$

2-5- FE-based simulation

The FEM is among the most widely used computational techniques for solving differential equations, particularly in nonlinear and complex problems. Lagrange interpolation functions ψ^e approximate the degrees of freedom [39].

$$\begin{aligned}u_0\left(x,y,t\right)&=\sum_{j=1}^{n}u_j\left(t\right)\cdot\psi_j^e\left(x,y\right)\\ v_0\left(x,y,t\right)&=\sum_{j=1}^{n}v_j\left(t\right)\cdot\psi_j^e\left(x,y\right)\end{aligned} \tag{14}$$

$$w_0(x,y,t)=\sum_{j=1}^{n} w_j(t)\cdot\psi_j^e(x,y)$$

$$\phi_x(x,y,t)=\sum_{j=1}^{n} S_j^1(t)\cdot\psi_j^e(x,y)$$

$$\phi_y(x,y,t)=\sum_{j=1}^{n} S_j^2(t)\cdot\psi_j^e(x,y)$$

A nine-node quadratic Lagrange rectangular element is used to approximate the interpolation functions. Fig. 6 illustrates the blade geometry, the adopted coordinate system, the finite element mesh, and the employed a nine-node quadratic Lagrange rectangular element.

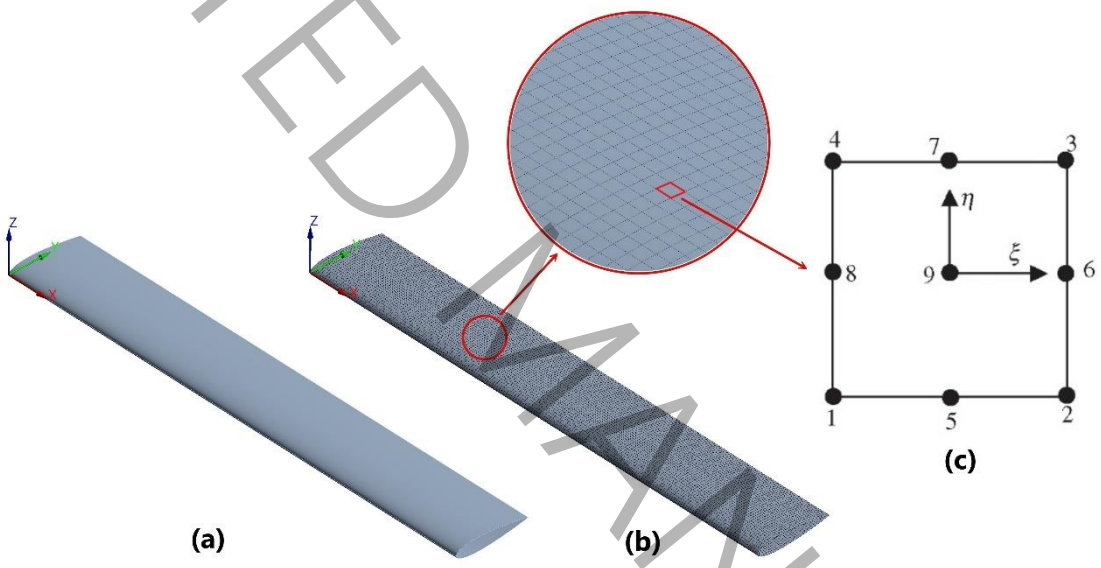

Fig. 6 Blade configuration; (a) geometry, (b) mesh, (c) an 9-node element

Following the application of the Galerkin method to transform the differential equations into a discrete form, the substitution of the degrees of freedom associated with the interpolation functions into these equations, and the transformation between the global and local coordinate, the equations of motion for each element are obtained in the following form.

$$\left[M^e\right]\cdot\left\{\ddot{\Delta}^e\right\}+\begin{pmatrix}\left[K_L^e\right]+\left[{}_1K_{NL}^e\right]\cdot\left(diag\left(\left\{w^e\right\}\right)\otimes I_5\right)\\+\left[{}_2K_{NL}^e\right]\cdot\left(diag\left(\left\{w^e\right\}^{\odot 2}\right)\otimes I_5\right)\end{pmatrix}\cdot\left\{\Delta^e\right\}=\{0\} \tag{15}$$

K_L^e, ${}_1K_{NL}^e$, ${}_2K_{NL}^e$, M^e, and Δ^e represent, respectively, the linear stiffness matrix, first and second nonlinear stiffness matrices, mass matrix, and the element displacement vector. The notations $\{\ \}$ and $\langle\ \rangle$ denote column and row matrices, respectively. The symbols $\otimes$ and $\odot$ represent the Kronecker and Hadamard products, respectively. The command diag transforms the column matrix $\{w\}$ into a diagonal matrix. I_5 denotes the 5×5 identity matrix. Each of these matrices (and vectors) is symbolically expressed below.

$$\left[M^e\right]=\begin{bmatrix} [M_{11}] & [0] & [0] & [M_{14}] & [0] \\ [0] & [M_{22}] & [0] & [0] & [M_{25}] \\ [0] & [0] & [M_{33}] & [0] & [0] \\ [M_{14}]^T & [0] & [0] & [M_{44}] & [0] \\ [0] & [M_{25}]^T & [0] & [0] & [M_{55}] \end{bmatrix} \tag{16}$$

$$\left[K_L^e\right]=\begin{bmatrix} \left[K_L^{11}\right] & \left[K_L^{12}\right] & \left[K_L^{13}\right] & \left[K_L^{14}\right] & \left[K_L^{15}\right] \\ \left[K_L^{12}\right]^T & \left[K_L^{22}\right] & \left[K_L^{23}\right] & \left[K_L^{24}\right] & \left[K_L^{25}\right] \\ \left[K_L^{13}\right]^T & \left[K_L^{23}\right]^T & \left[K_L^{33}\right] & \left[K_L^{34}\right] & \left[K_L^{35}\right] \\ \left[K_L^{14}\right]^T & \left[K_L^{24}\right]^T & \left[K_L^{34}\right]^T & \left[K_L^{44}\right] & \left[K_L^{45}\right] \\ \left[K_L^{15}\right]^T & \left[K_L^{25}\right]^T & \left[K_L^{35}\right]^T & \left[K_L^{45}\right]^T & \left[K_L^{55}\right] \end{bmatrix} \tag{17}$$

$$\left[{}_1K_{NL}^e\right]=\begin{bmatrix} [0] & [0] & \left[{}_1K_{NL}^{13}\right] & [0] & [0] \\ [0] & [0] & \left[{}_1K_{NL}^{23}\right] & [0] & [0] \\ \left[{}_1K_{NL}^{31}\right] & \left[{}_1K_{NL}^{32}\right] & \left[{}_1K_{NL}^{33}\right] & \left[{}_1K_{NL}^{34}\right] & \left[{}_1K_{NL}^{35}\right] \\ [0] & [0] & \left[{}_1K_{NL}^{43}\right] & [0] & [0] \\ [0] & [0] & \left[{}_1K_{NL}^{53}\right] & [0] & [0] \end{bmatrix} \tag{18}$$

$$\left[{}_2K_{NL}^e\right]=\begin{bmatrix} [0] & [0] & [0] & [0] & [0] \\ [0] & [0] & [0] & [0] & [0] \\ [0] & [0] & \left[{}_2K_{NL}^{33}\right] & [0] & [0] \\ [0] & [0] & [0] & [0] & [0] \\ [0] & [0] & [0] & [0] & [0] \end{bmatrix} \tag{19}$$

$$\left\{\Delta^e\right\}=\begin{bmatrix} \langle u\rangle & \langle v\rangle & \langle w\rangle & \left\langle S^1\right\rangle & \left\langle S^2\right\rangle \end{bmatrix}^T \tag{20}$$

The entries of the element stiffness and mass matrices are calculated as follows. The parameter α ranges from 1 to 5.

$$K_{L_{ij}}^{1\alpha} = \int_{\gamma_e} \left[\psi_{i,x}^e \cdot N_{xxL_j}^{\alpha} + \psi_{i,y}^e \cdot \left(N_{xyL_j}^{\alpha} + C_0 \cdot M_{xyL_j}^{\alpha} \right) - \psi_i^e \cdot \frac{Q_{x_j}^{\alpha}}{R_1} \right] \cdot dx \cdot dy \tag{21}$$

$$K_{L_{ij}}^{2\alpha} = \int_{\gamma_e} \left[\psi_{i,x}^e \cdot \left(N_{xyL_j}^{\alpha} - C_0 \cdot M_{xyL_j}^{\alpha} \right) + \psi_{i,y}^e \cdot N_{yyL_j}^{\alpha} - \psi_i^e \cdot \frac{Q_{y_j}^{\alpha}}{R_2} \right] \cdot dx \cdot dy \tag{22}$$

$$K_{L_{ij}}^{3\alpha} = \int_{\gamma_e} \left[\psi_{i,x}^e \cdot Q_{x_j}^{\alpha} + \psi_{i,y}^e \cdot Q_{y_j}^{\alpha} + \psi_i^e \cdot \left(\frac{N_{xxL_j}^{\alpha}}{R_1} + \frac{N_{yyL_j}^{\alpha}}{R_2} \right) \right] \cdot dx \cdot dy \tag{23}$$

$$K_{L_{ij}}^{4\alpha} = \int_{\gamma_e} \left[\psi_{i,x}^e \cdot M_{xxL_j}^{\alpha} + \psi_{i,y}^e \cdot M_{xyL_j}^{\alpha} + \psi_i^e \cdot Q_{x_j}^{\alpha} \right] \cdot dx \cdot dy \tag{24}$$

$$K_{L_{ij}}^{5\alpha} = \int_{\gamma_e} \left[\psi_{i,x}^e \cdot M_{xyL_j}^{\alpha} + \psi_{i,y}^e \cdot M_{yyL_j}^{\alpha} + \psi_i^e \cdot Q_{y_j}^{\alpha} \right] \cdot dx \cdot dy \tag{25}$$

$${}_1K_{NL_{ij}}^{13} = \int_{\gamma_e} \left[\psi_{i,x}^e \cdot N_{xxNL_j}^{3} + \psi_{i,y}^e \cdot \left(N_{xxNL_j}^{3} + C_0 \cdot M_{xyNL_j}^{3} \right) \right] \cdot dx \cdot dy \tag{26}$$

$${}_1K_{NL_{ij}}^{23} = \int_{\gamma_e} \left[\psi_{i,x}^e \cdot \left(N_{xyNL_j}^{3} - C_0 \cdot M_{xyNL_j}^{3} \right) + \psi_{i,y}^e \cdot N_{yyNL_j}^{3} \right] \cdot dx \cdot dy \tag{27}$$

$${}_1K_{NL_{ij}}^{3\alpha} = \int_{\gamma_e} \left[\begin{array}{l} \psi_{i,x}^e \cdot \left(N_{xxL_j}^{\alpha} \cdot \psi_{j,x}^e + N_{xyL_j}^{\alpha} \cdot \psi_{j,y}^e \right) + \psi_{i,y}^e \cdot \left(N_{xyL_j}^{\alpha} \cdot \psi_{j,x}^e + N_{yyL_j}^{\alpha} \cdot \psi_{j,y}^e \right) \\ + \psi_i^e \cdot \left(\dfrac{N_{xxNL_j}^{\alpha}}{R_1} + \dfrac{N_{yyNL_j}^{\alpha}}{R_2} \right) \end{array} \right] \cdot dx \cdot dy \tag{28}$$

$${}_1K_{NL_{ij}}^{43} = \int_{\gamma_e} \left[\psi_{i,x}^e \cdot M_{xxNL_j}^{3} + \psi_{i,y}^e \cdot M_{xyNL_j}^{3} \right] \cdot dx \cdot dy \tag{29}$$

$${}_1K_{NL_{ij}}^{53} = \int_{\gamma_e} \left[\psi_{i,x}^e \cdot M_{xyNL_j}^{3} + \psi_{i,y}^e \cdot M_{yyNL_j}^{3} \right] \cdot dx \cdot dy \tag{30}$$

$${}_2K_{NL_{ij}}^{3\alpha} = \int_{\gamma_e} \left[\psi_{i,x}^e \cdot \left(N_{xxNL_j}^{\alpha} \cdot \psi_{j,x}^e + N_{xyNL_j}^{\alpha} \cdot \psi_{j,y}^e \right) + \psi_{i,y}^e \cdot \left(N_{xyNL_j}^{\alpha} \cdot \psi_{j,x}^e + N_{yyNL_j}^{\alpha} \cdot \psi_{j,y}^e \right) \right] \cdot dx \cdot dy \tag{31}$$

$$M_{ij}^{11} = M_{ij}^{22} = M_{ij}^{33} = I_0 \cdot \int_{\gamma_e} \psi_i^e \cdot \psi_j^e \cdot dx \cdot dy \tag{32}$$

$$M_{ij}^{14} = M_{ij}^{25} = I_1 \cdot \int_{\gamma_e} \psi_i^e \cdot \psi_j^e \cdot dx \cdot dy \tag{33}$$

$$M_{ij}^{44} = M_{ij}^{55} = I_2 \cdot \int_{\gamma_e} \psi_i^e \cdot \psi_j^e \cdot dx \cdot dy \tag{34}$$

Here, the element area $dA = dx \cdot dy$ in the element γ^e is transformed into the area $dA = |J| \cdot d\xi \cdot d\eta$ in the reference element $\hat{\gamma} = \{(\xi, \eta) : -1 \le \xi \le 1, -1 \le \eta \le 1\}$. The $|J|$ represents the determinant of the Jacobian matrix, and J^* denotes the inverse of the Jacobian matrix. The Jacobian matrix is written as follows.

$$[J]=\begin{bmatrix} \frac{\partial \hat{\psi}_1}{\partial \xi} & \frac{\partial \hat{\psi}_2}{\partial \xi} & \cdots & \frac{\partial \hat{\psi}_m}{\partial \xi} \\ \frac{\partial \hat{\psi}_1}{\partial \eta} & \frac{\partial \hat{\psi}_2}{\partial \eta} & \cdots & \frac{\partial \hat{\psi}_m}{\partial \eta} \end{bmatrix} \begin{bmatrix} x_1 & y_1 \\ x_2 & y_2 \\ \vdots & \vdots \\ x_m & y_m \end{bmatrix} \tag{35}$$

The $\hat{\psi}^e$ is the linear Lagrange rectangular element interpolation function for geometry approximation. Accordingly, the partial derivatives of the interpolation functions ψ^e in terms of x and y are expressed as follows.

$$\begin{Bmatrix} \frac{\partial \psi_i^e}{\partial x} \\ \frac{\partial \psi_i^e}{\partial y} \end{Bmatrix} = \left[J^* \right] \begin{Bmatrix} \frac{\partial \psi_i^e}{\partial \xi} \\ \frac{\partial \psi_i^e}{\partial \eta} \end{Bmatrix} \tag{36}$$

The non-zero coefficients present in the element matrices (stiffness and mass) are defined based on the following relationships.

$$N^1_{xxL_j} = A_{11} \cdot \psi^e_{j,x} + A_{16} \cdot \psi^e_{j,y} \tag{37}$$
$$N^2_{xxL_j} = A_{16} \cdot \psi^e_{j,x} + A_{12} \cdot \psi^e_{j,y} \tag{38}$$
$$N^3_{xxL_j} = \left(\frac{A_{11}}{R_1} + \frac{A_{12}}{R_2} \right) \cdot \psi^e_j \tag{39}$$
$$N^4_{xxL_j} = B_{11} \cdot \psi^e_{j,x} + B_{16} \cdot \psi^e_{j,y} \tag{40}$$
$$N^5_{xxL_j} = B_{16} \cdot \psi^e_{j,x} + B_{12} \cdot \psi^e_{j,y} \tag{41}$$
$$N^1_{xyL_j} = A_{16} \cdot \psi^e_{j,x} + A_{66} \cdot \psi^e_{j,y} \tag{42}$$
$$N^2_{xyL_j} = A_{66} \cdot \psi^e_{j,x} + A_{26} \cdot \psi^e_{j,y} \tag{43}$$
$$N^3_{xyL_j} = \left(\frac{A_{16}}{R_1} + \frac{A_{26}}{R_2} \right) \cdot \psi^e_j \tag{44}$$
$$N^4_{xyL_j} = B_{16} \cdot \psi^e_{j,x} + B_{66} \cdot \psi^e_{j,y} \tag{45}$$
$$N^5_{xyL_j} = B_{66} \cdot \psi^e_{j,x} + B_{26} \cdot \psi^e_{j,y} \tag{46}$$
$$N^1_{yyL_j} = A_{12} \cdot \psi^e_{j,x} + A_{26} \cdot \psi^e_{j,y} \tag{47}$$
$$N^2_{yyL_j} = A_{26} \cdot \psi^e_{j,x} + A_{22} \cdot \psi^e_{j,y} \tag{48}$$

$$N^{3}_{yyL_j} = \left(\frac{A_{12}}{R_1} + \frac{A_{22}}{R_2} \right) \cdot \psi^{e}_{j} \tag{49}$$

$$N^{4}_{yyL_j} = B_{12} \cdot \psi^{e}_{j,x} + B_{26} \cdot \psi^{e}_{j,y} \tag{50}$$

$$N^{5}_{yyL_j} = B_{26} \cdot \psi^{e}_{j,x} + B_{22} \cdot \psi^{e}_{j,y} \tag{51}$$

$$M^{1}_{xxL_j} = B_{11} \cdot \psi^{e}_{j,x} + B_{16} \cdot \psi^{e}_{j,y} \tag{52}$$

$$M^{2}_{xxL_j} = B_{16} \cdot \psi^{e}_{j,x} + B_{12} \cdot \psi^{e}_{j,y} \tag{53}$$

$$M^{3}_{xxL_j} = \left(\frac{B_{11}}{R_1} + \frac{B_{12}}{R_2} \right) \cdot \psi^{e}_{j} \tag{54}$$

$$M^{4}_{xxL_j} = D_{11} \cdot \psi^{e}_{j,x} + D_{16} \cdot \psi^{e}_{j,y} \tag{55}$$

$$M^{5}_{xxL_j} = D_{16} \cdot \psi^{e}_{j,x} + D_{12} \cdot \psi^{e}_{j,y} \tag{56}$$

$$M^{1}_{xyL_j} = B_{16} \cdot \psi^{e}_{j,x} + B_{66} \cdot \psi^{e}_{j,y} \tag{57}$$

$$M^{2}_{xyL_j} = B_{66} \cdot \psi^{e}_{j,x} + B_{26} \cdot \psi^{e}_{j,y} \tag{58}$$

$$M^{3}_{xyL_j} = \left(\frac{B_{16}}{R_1} + \frac{B_{26}}{R_2} \right) \cdot \psi^{e}_{j} \tag{59}$$

$$M^{4}_{xyL_j} = D_{16} \cdot \psi^{e}_{j,x} + D_{66} \cdot \psi^{e}_{j,y} \tag{60}$$

$$M^{5}_{xyL_j} = D_{66} \cdot \psi^{e}_{j,x} + D_{26} \cdot \psi^{e}_{j,y} \tag{61}$$

$$M^{1}_{yyL_j} = B_{12} \cdot \psi^{e}_{j,x} + B_{26} \cdot \psi^{e}_{j,y} \tag{62}$$

$$M^{2}_{yyL_j} = B_{26} \cdot \psi^{e}_{j,x} + B_{22} \cdot \psi^{e}_{j,y} \tag{63}$$

$$M^{3}_{yyL_j} = \left(\frac{B_{12}}{R_1} + \frac{B_{22}}{R_2} \right) \cdot \psi^{e}_{j} \tag{64}$$

$$M^{4}_{yyL_j} = D_{12} \cdot \psi^{e}_{j,x} + D_{26} \cdot \psi^{e}_{j,y} \tag{65}$$

$$M^{5}_{yyL_j} = D_{26} \cdot \psi^{e}_{j,x} + D_{22} \cdot \psi^{e}_{j,y} \tag{66}$$

$$Q^{1}_{x_j} = -\frac{K_s \cdot A_{55}}{R_1} \cdot \psi^{e}_{j} \tag{67}$$

$$Q^{2}_{x_j} = -\frac{K_s \cdot A_{45}}{R_2} \cdot \psi^{e}_{j} \tag{68}$$

$$Q^{3}_{x_j} = K_s \cdot \left(A_{55} \cdot \psi^{e}_{j,x} + A_{45} \cdot \psi^{e}_{j,y} \right) \tag{69}$$

$$Q^{4}_{x_j} = K_s \cdot A_{55} \cdot \psi^{e}_{j} \tag{70}$$

$$Q^{5}_{x_j} = K_s \cdot A_{45} \cdot \psi^{e}_{j} \tag{71}$$

$$Q^{1}_{y_j} = -\frac{K_s \cdot A_{45}}{R_1} \cdot \psi^{e}_{j} \tag{72}$$

$$Q^{2}_{y_j} = -\frac{K_s \cdot A_{44}}{R_2} \cdot \psi^{e}_{j} \tag{73}$$

$$Q^{3}_{y_j} = K_s \cdot \left(A_{45} \cdot \psi^{e}_{j,x} + A_{44} \cdot \psi^{e}_{j,y} \right) \tag{74}$$

$$Q_{y_j}^4 = K_s \cdot A_{45} \cdot \psi_j^e \tag{75}$$

$$Q_{y_j}^5 = K_s \cdot A_{44} \cdot \psi_j^e \tag{76}$$

$$N_{xxNL_j}^3 = \frac{1}{2} \cdot \left(A_{11} \cdot {\psi_{j,x}^e}^2 + A_{12} \cdot {\psi_{j,y}^e}^2 + 2 \cdot A_{16} \cdot \psi_{j,x}^e \cdot \psi_{j,y}^e \right) \tag{77}$$

$$N_{xyNL_j}^3 = \frac{1}{2} \cdot \left(A_{16} \cdot {\psi_{j,x}^e}^2 + A_{26} \cdot {\psi_{j,y}^e}^2 + 2 \cdot A_{66} \cdot \psi_{j,x}^e \cdot \psi_{j,y}^e \right) \tag{78}$$

$$N_{yyNL_j}^3 = \frac{1}{2} \cdot \left(A_{12} \cdot {\psi_{j,x}^e}^2 + A_{22} \cdot {\psi_{j,y}^e}^2 + 2 \cdot A_{26} \cdot \psi_{j,x}^e \cdot \psi_{j,y}^e \right) \tag{79}$$

$$M_{xxNL_j}^3 = \frac{1}{2} \cdot \left(B_{11} \cdot {\psi_{j,x}^e}^2 + B_{12} \cdot {\psi_{j,y}^e}^2 + 2 \cdot B_{16} \cdot \psi_{j,x}^e \cdot \psi_{j,y}^e \right) \tag{80}$$

$$M_{xyNL_j}^3 = \frac{1}{2} \cdot \left(B_{16} \cdot {\psi_{j,x}^e}^2 + B_{26} \cdot {\psi_{j,y}^e}^2 + 2 \cdot B_{66} \cdot \psi_{j,x}^e \cdot \psi_{j,y}^e \right) \tag{81}$$

$$M_{yyNL_j}^3 = \frac{1}{2} \cdot \left(B_{12} \cdot {\psi_{j,x}^e}^2 + B_{22} \cdot {\psi_{j,y}^e}^2 + 2 \cdot B_{26} \cdot \psi_{j,x}^e \cdot \psi_{j,y}^e \right) \tag{82}$$

A, *B*, and *D* represent the laminated stiffness matrices corresponding to in-plane, coupling, and bending stiffness, respectively. To accurately calculate each integral over the interval [-1, 1], the Gauss quadrature numerical integration method is employed [48].

Note that the blade geometry is modeled as a shell with single curvature. Accordingly, the radius of curvature along the x (or span-wise) direction is considered infinite, leading to the following conclusion.

$$R_1 \to \infty, \qquad \frac{1}{R_1} \approx 0 \tag{83}$$

And the radius of curvature along the y (or chord wise) direction of the NACA 0018 airfoil is obtained from the airfoil curve equation $z_{af}(y)$ as follows.

$$z_{af}(y) = 5 \cdot t \cdot \left(0.2969 \cdot \sqrt{\bar{y}} - 0.126 \cdot \bar{y} - 0.3516 \cdot \bar{y}^2 + 0.2843 \cdot \bar{y}^3 - 0.1036 \cdot \bar{y}^4 \right) \tag{84}$$

$$R_2 = \frac{\left(1 + z_{af,y}\right)^{\frac{3}{2}}}{z_{af,yy}}, \qquad \bar{y} = \frac{y}{c} \tag{85}$$

The *c* is the blade chord length, and *t* is the maximum thickness as a fraction of the chord, and equals 0.18. After meshing the blade shell and defining the element and node numbers, each element's mass and stiffness matrices are assembled to obtain the entire blade structure's global mass and stiffness matrices. Accordingly, the governing equation of motion for the entire structure is obtained as follows.

$$[M]\cdot\{\ddot{\Delta}\}+\begin{pmatrix}[K_L]+[{}_1K_{NL}]\cdot\left(diag\left(\{w\}\right)\otimes I_5\right)\\+[{}_2K_{NL}]\cdot\left(diag\left(\{w\}^{\odot 2}\right)\otimes I_5\right)\end{pmatrix}\cdot\{\Delta\}=\{0\} \tag{86}$$

The clamped (C) boundary conditions at the root of the blade location are [48]

$$C: u_0=v_0=w_0=\phi_x=\phi_y=0 \tag{87}$$

In structures with fixed-free boundary conditions, such as cantilever beams or shells, the primary source of nonlinearity is attributed to large-amplitude deformations, specifically non-linear inertia and the non-linear contribution to bending curvature, rather than tensile stretching. This shift occurs because the free end of the structure can undergo large displacements, allowing it to behave as inextensional up to a high order of approximation. In contrast, structures with a fixed distance between supports (such as clamped-clamped or pinned-pinned beams) are dominated by mid-plane stretching because their axial motion is constrained, inducing significant tensile effects. Because a fixed-free structure lacks these axial constraints, it does not experience the same stretching-induced nonlinearities, leaving geometric and inertial effects as the governing nonlinear factors in its motion [49, 50].

2-6- Nonlinear free vibration analysis

The nonlinear free vibration analysis results are represented using a backbone curve, which captures the relationship between the system's peak amplitude and natural frequency. When the natural frequency rises with increasing amplitude, the system exhibits hardening behavior; conversely, a decrease in frequency with amplitude indicates softening. The importance of increasing nonlinear hardening behavior and achieving a lower peak amplitude in the 2DTBC blade is rooted in enhancing structural

rigidity and ensuring accurate prediction of dynamic responses under large excitations. So, in the case of composite blades, enhancing hardening behavior is generally preferred [51].

The hardening behavior of a structure, as illustrated by its backbone curve, describes a physical state where the system's resistance or stiffness increases as it undergoes larger deformations or oscillations. In the context of nonlinear vibrations, a backbone curve defines the natural frequency as a function of the response amplitude when damping and forcing are absent. Physically, the greater the deformation of the structure, the greater the resistance the structure will show to this deformation. This behavior provides vital insight into system dynamics, enabling engineers to characterize active nonlinearities and make appropriate estimates of the actual deformation of the structure during design.

The Harmonic Balance Method (HBM), often referred to as the Fourier–Galerkin approach, stands as one of the cornerstone techniques in the frequency-domain analysis of nonlinear dynamic systems. It is an approximation method for computing periodic solutions of nonlinear ordinary differential equations (ODEs) [52-54].

At the heart of the HBM lies the idea of representing the time-dependent system response, such as displacement, as a truncated Fourier series composed of a finite number of sine and cosine terms. This Fourier representation captures the essential periodic nature of the response. The assumed solution is then substituted into the system’s equation of motion, after which the coefficients of identical harmonic terms are equated or balanced [52, 55-57]. Through this balancing process, the original nonlinear differential equation is systematically converted into a group of nonlinear algebraic equations represented in the frequency domain [55, 57]. Solving these algebraic equations yields the unknown Fourier coefficients, which describe the system’s steady-state oscillations [52, 56].

A major advantage of HBM is its ability to handle strongly nonlinear systems, in contrast to traditional perturbation-based methods that are restricted to weakly nonlinear cases [52, 55]. For smooth nonlinearities, the method often produces solutions that closely approximate — and in many cases converge to — the exact periodic response. This makes HBM a powerful analytical and semi-analytical tool in the study of nonlinear vibrations and dynamical systems. However, the accuracy of the Harmonic

Balance Method depends heavily on the number of harmonics retained in the Fourier expansion. Increasing this number improves the fidelity of the approximation, but at a significant computational cost. In recent years, advances in computational techniques have helped mitigate these challenges. Tools such as automatic differentiation, symbolic–numeric hybrid solvers, and parallelized algorithms have been introduced to enhance the efficiency of the HBM framework. These innovations have considerably expanded the method's applicability, enabling researchers to analyze high-dimensional and strongly nonlinear systems that were once beyond its reach [52].

Initially, the equation of motion of the structure, i.e., relation Eq. (86), is expanded as follows by neglecting the in-plane inertia terms [55, 58, 59].

$$\left[M_{33}\right]\cdot\left\{\ddot{w}\right\}+\left[K_L^{33}\right]\cdot\left\{w\right\}+\left[{}_1K_{NL}^{33}\right]\cdot\left\{w\right\}^{\odot 2}+\left[{}_2K_{NL}^{33}\right]\cdot\left\{w\right\}^{\odot 3}=\left\{0\right\} \tag{88}$$

The vector of degrees of freedom $\left\{w\right\}$, is now expressed in terms of the Fourier series as follows.

$$\left\{w\right\}=\sum_{n=1}^{N_H}\left\{c_n^w\right\}\cdot\cos\left(n\cdot\omega\cdot t\right)+\sum_{n=1}^{N_H}\left\{s_n^w\right\}\cdot\sin\left(n\cdot\omega\cdot t\right) \tag{89}$$

The initial conditions of the problem are assumed as follows.

$$\left\{w(0)\right\}=\left\{w_0\right\},\qquad \left\{\dot{w}(0)\right\}=\left\{0\right\} \tag{90}$$

By substituting the initial conditions into the Fourier series of Eq. (89), it is concluded that the coefficient of the sine term, denoted by $\left\{s_n^w\right\}$, is always zero. Therefore, for the two cosine terms, i.e., $N_H=2$, one can write

$$\left\{w\right\}=\left\{c_1^w\right\}\cdot\cos\left(\omega\cdot t\right)+\left\{c_2^w\right\}\cdot\cos\left(2\cdot\omega\cdot t\right) \tag{91}$$

By substituting Eq. (91) into Eqs. (89) and (90), and simplifying, the following harmonic equations can be obtained.

$$\begin{pmatrix} -\omega^2 \cdot \left(\left[M_{33} \right] + \left[K_L^{33} \right] \right) \cdot \left\{ c_1^w \right\} + \left[{}_1K_{NL}^{33} \right] \cdot \left\{ \left\{ c_1^w \right\} \odot \left\{ c_2^w \right\} \right\} \\ + \frac{3}{4} \cdot \left[{}_2K_{NL}^{33} \right] \cdot \left\{ c_1^w \right\}^{\odot 3} + \frac{3}{2} \cdot \left[{}_2K_{NL}^{33} \right] \cdot \left\{ \left\{ c_1^w \right\} \odot \left\{ c_2^w \right\}^{\odot 2} \right\} \end{pmatrix} \cdot \cos\left(\omega \cdot t \right) + \begin{pmatrix} -4 \cdot \omega^2 \cdot \left(\left[M_{33} \right] + \left[K_L^{33} \right] \right) \cdot \left\{ c_2^w \right\} + \frac{1}{2} \cdot \left[{}_1K_{NL}^{33} \right] \cdot \left\{ c_1^w \right\}^{\odot 2} \\ + \frac{3}{2} \cdot \left[{}_2K_{NL}^{33} \right] \cdot \left\{ \left\{ c_1^w \right\}^{\odot 2} \odot \left\{ c_2^w \right\} \right\} + \frac{3}{4} \cdot \left[{}_2K_{NL}^{33} \right] \cdot \left\{ c_2^w \right\}^{\odot 3} \end{pmatrix} \cdot \cos\left(2 \cdot \omega \cdot t \right) + HOH \approx \left\{ 0 \right\} \tag{92}$$

$$\left\{ c_1^w \right\} + \left\{ c_2^w \right\} = \left\{ w_0 \right\} \tag{93}$$

Where HOH denotes the higher-order harmonics. By setting the coefficients of the $\cos\left(\omega \cdot t \right)$ and $\cos\left(2 \cdot \omega \cdot t \right)$ terms to zero, along with the equation derived from the initial condition, a system of three equations with three unknowns is finally obtained as follows.

$$-\omega^2 \cdot \left(\left[M_{33} \right] + \left[K_L^{33} \right] \right) \cdot \left\{ c_1^w \right\} + \left[{}_1K_{NL}^{33} \right] \cdot \left\{ \left\{ c_1^w \right\} \odot \left\{ c_2^w \right\} \right\} + \frac{3}{4} \cdot \left[{}_2K_{NL}^{33} \right] \cdot \left\{ c_1^w \right\}^{\odot 3} + \frac{3}{2} \cdot \left[{}_2K_{NL}^{33} \right] \cdot \left\{ \left\{ c_1^w \right\} \odot \left\{ c_2^w \right\}^{\odot 2} \right\} = \left\{ 0 \right\} \tag{94}$$

$$-4 \cdot \omega^2 \cdot \left(\left[M_{33} \right] + \left[K_L^{33} \right] \right) \cdot \left\{ c_2^w \right\} + \frac{1}{2} \cdot \left[{}_1K_{NL}^{33} \right] \cdot \left\{ c_1^w \right\}^{\odot 2} + \frac{3}{2} \cdot \left[{}_2K_{NL}^{33} \right] \cdot \left\{ \left\{ c_1^w \right\}^{\odot 2} \odot \left\{ c_2^w \right\} \right\} + \frac{3}{4} \cdot \left[{}_2K_{NL}^{33} \right] \cdot \left\{ c_2^w \right\}^{\odot 3} = \left\{ 0 \right\} \tag{95}$$

$$\left\{ c_1^w \right\} + \left\{ c_2^w \right\} - \left\{ w_0 \right\} = \left\{ 0 \right\} \tag{96}$$

By solving this system of equations, the unknown variables $\left\{ c_1^w \right\}$, $\left\{ c_2^w \right\}$, and $\left\{ \omega \right\}$ are obtained. Finally, by plotting the amplitude $\left\{ w_0 \right\}$, versus frequency $\left\{ \omega \right\}$, the backbone curve is derived.

2-7- GA-based optimization

This research employed the conventional single-objective genetic algorithm method to conduct the optimization process. The optimization variables included braiding angle, braiding space, yarn count,

and the number of layers. During the optimization procedure, the algorithm's The hyper-parameters were set and adjusted as listed in Table 5.

Table 5. Hyperparameters of single-objective genetic algorithm.

Parameter	Value
Pareto fraction	100% of population size
Maximum generation	80
Population size	80
Population type	Double vector
Creation function	Constraint dependent
Selection function	Tournament
Selection size	1
Mutation function	Adapt feasible
Mutation fraction	0.20
Crossover function	Two points
Crossover fraction	0.8

The aim here is to improve the hardening behavior of the composite blade. This behavior is represented by a backbone curve, with the vertical axis showing the oscillation amplitude and the horizontal axis showing the natural frequency (Fig. 7).

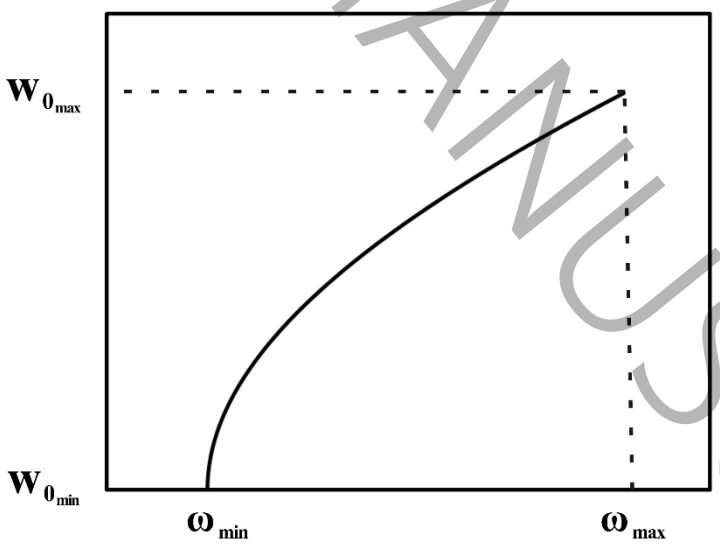

Fig. 7: Schematic illustration of the backbone curve

In the optimization process, the amplitude is not necessarily constant, as the genetic algorithm evaluates various layer configurations. In some configurations, the structural stiffness may increase significantly, which necessitates considering larger amplitude ranges. Therefore, the amplitude range is not fixed for each layer configuration. To establish a consistent and uniform criterion for comparison across different configurations, the amplitude-to-frequency ratio was selected as the objective function. While in some cases the amplitude may remain approximately constant, this does not contradict the use of this fractional ratio as a meaningful measure. Accordingly, the objective function is defined as follows to achieve this enhancement.

$$f(x)=\frac{w_{0_{\max}}-w_{0_{\min}}}{\omega_{\max}-\omega_{\min}}:\quad R^{25}\to R\quad find\ \bar{x}\in R^{25}\ such\ that\ f(\bar{x})\le f(x) \tag{97}$$

Subjected to

$$x=\left\{N,\underbrace{V_t,V_c,C,D}_{3\text{ to }6\text{ times}}\right\} \tag{98}$$

$\left(\omega_{\min},w_{0_{\min}}\right)$ are the smallest natural frequency and amplitude of the backbone curve and $\left(\omega_{\max},w_{0_{\max}}\right)$ are the largest natural frequency and amplitude of the backbone curve. *x* is a vector that stores the optimization parameters. The parameters V_t,V_c,C,D,N represent the take-off speed, carrier speed, chord length, yarn count, and the number of layers, respectively.

Considering that the number of braid layers can vary between 3 and 6, the second term within the parentheses, i.e., $\left(V_t,V_c,C,D\right)$, is repeated for each layer in the optimization process. Therefore, in the most extensive case (for six layers), this section is repeated 6 times, forming a chromosome with a total length of 25 genes alongside the other parameters.

It is worth noting that the optimization process was implemented and executed using MATLAB software.

3- Results and discussions

3-1- ANN prediction quality

Fig. 8 presents the predictive performance of the ANN models for establishing the relationship between the braiding machine parameters and the resulting braided structure for the training and testing stages, respectively. The predictive performance of the models was exceptionally high, demonstrating a perfect correlation between actual and predicted values, as reflected by a correlation coefficient of 100%.

In addition, Fig. 8(c), (d) illustrate the model's precise predictions for braiding space during both phases, while Fig. 8(e), (f) show similarly accurate results for the braiding angle. The close alignment between predicted and actual values in all these plots highlights the model's robustness in capturing the complex relationships between input parameters and structural outcomes. This is further substantiated by the consistently high coefficient of determination (R^2) values. Crucially, the model's high predictive performance is not confined to isolated portions of the dataset; instead, it has been observed uniformly across the entire range of data, confirming the ANN model's generalizability and reliability.

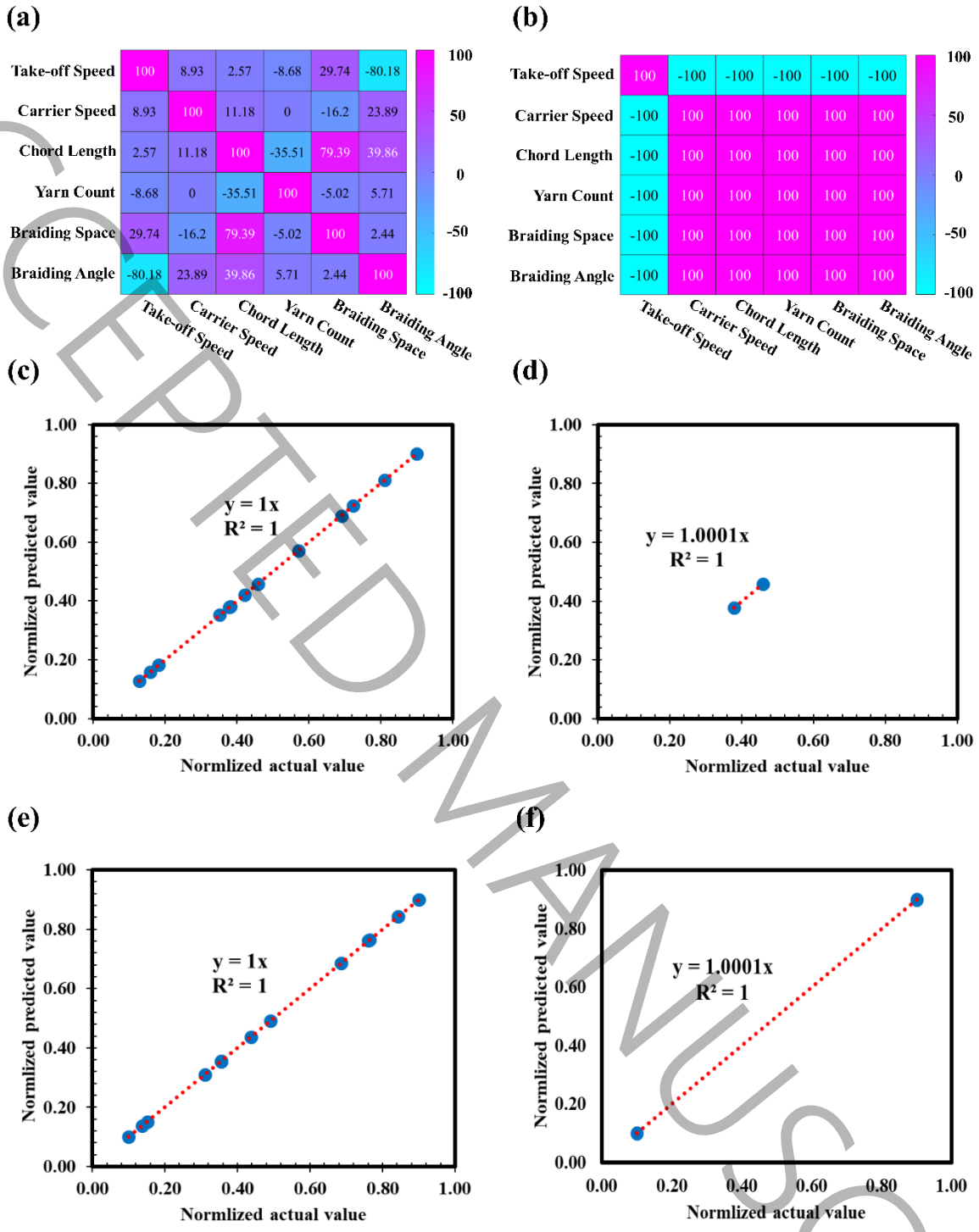

Fig. 8 Pearson's correlation heatmap matrix; (a) training step, (b) testing step, and goodness of fit between normalized actual and predicted values, (c) training step of braiding space, (d) testing step of braiding space, (e) training step of braiding angle, (f) testing step of braiding angle [39]

3-2- Performance of FE model

In the FEM analysis, a process known as a Mesh Study is employed to evaluate the precision and consistency of the results. This study aims to determine the optimal number of elements needed to

achieve accurate and stable results. If the number of elements is too small, the accuracy of the analysis decreases, and the obtained results will deviate from reality. Conversely, using an excessive number of elements may increase the computational cost and affect the accuracy of the results due to the accumulation of numerical errors. Therefore, to ensure that the dynamic response of the blade is independent of the mesh size and that further mesh refinement does not significantly affect the results, performing a mesh study is essential.

For this analysis, the process begins with a relatively coarse initial mesh, which is then gradually refined. A modal analysis is carried out for each mesh size, and the first transverse natural frequency of the blade is recorded. The mesh is deemed optimal when further refinement produces negligible variation in the computed natural frequency. Fig. 9 presents the natural frequency diagram of the blade structure for various mesh sizes. This blade is made up of three layers of epoxy glass braid with angles of 77.4, 43, and 43 degrees, [39].

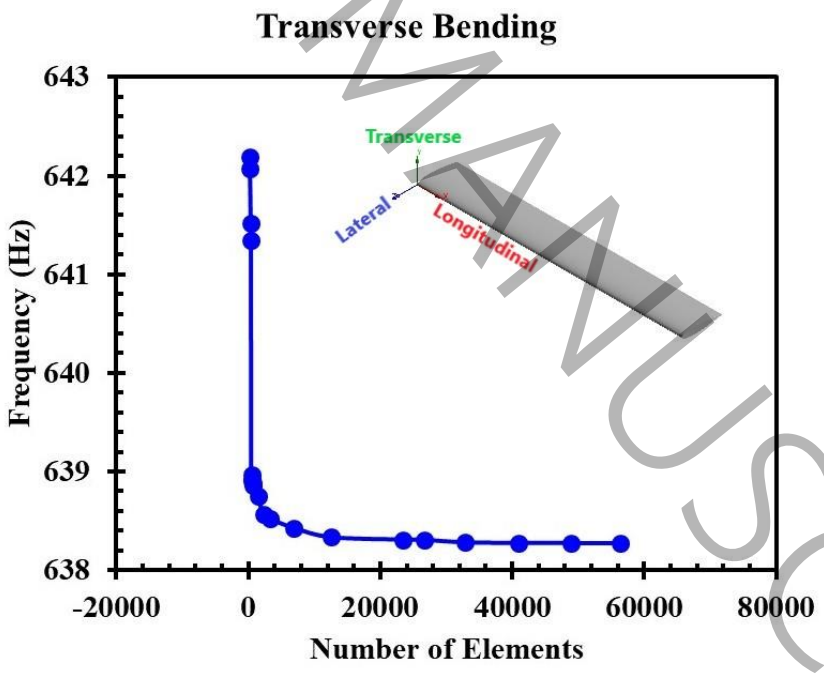

Fig. 9 Mesh convergence curve for transverse bending mode [39]

Based on the mesh study conducted, it was determined that utilizing 12540 elements establishes a suitable balance between the solution accuracy and computational expense. At this element count, the

variations in natural frequency compared to cases with finer meshes were negligible, indicating the convergence of the results and the adequacy of the numerical modeling accuracy.

To ensure the accuracy of the derived mathematical relationships for calculating the entries of the stiffness and mass matrices and the correctness of their implementation in the code, the results were validated against a reputable source. For this purpose, the nonlinear transient response of an isotropic square plate reported by Reddy [48], served as the basis for comparison. In this problem, all four edges of the plate were considered simply supported, and a permanent uniform step load was suddenly applied to the plate's surface. The geometric specifications, material properties, and load magnitude are provided in Table 6.

Table 6 geometric specifications and material properties of the isotropic square plate [48]

Parameter	Value
Length (cm)	243.8
Width (cm)	243.8
Thickness (cm)	0.635
Density (Kg/m3)	254.7
Young modulus (Gpa)	7.031
Poisson ratio	0.25
Load (Pa)	4.882

Fig. 10 depicts the displacement-time history of the plate's center for different numbers of elements, compared with the results reported by Reddy. This comparison reveals a maximum error of less than 4% for 10404 elements, with a significant portion of the two curves exhibiting acceptable agreement.

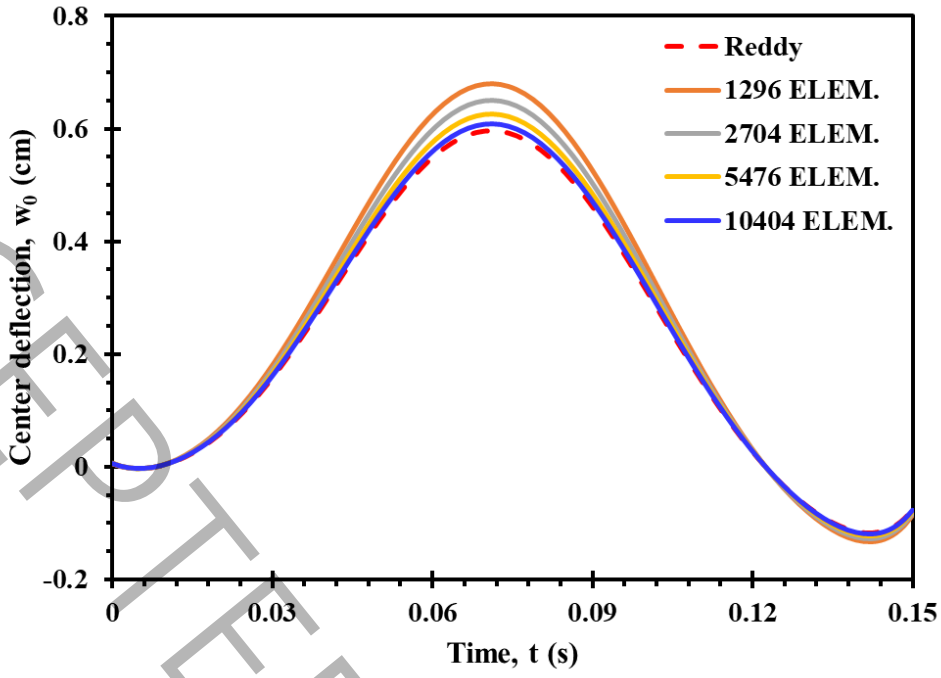

Fig. 10 Mesh study of the nonlinear transient response of center deflection in the simply supported isotropic square plate

Recognizing that cantilevered shells may exhibit higher sensitivity in nonlinear dynamic responses, an additional mesh convergence study has been performed specifically for a clamped cross-ply (0/90) laminated cylindrical shell panel under uniform load. The geometric characteristics of the shell are shown in Fig. 11.

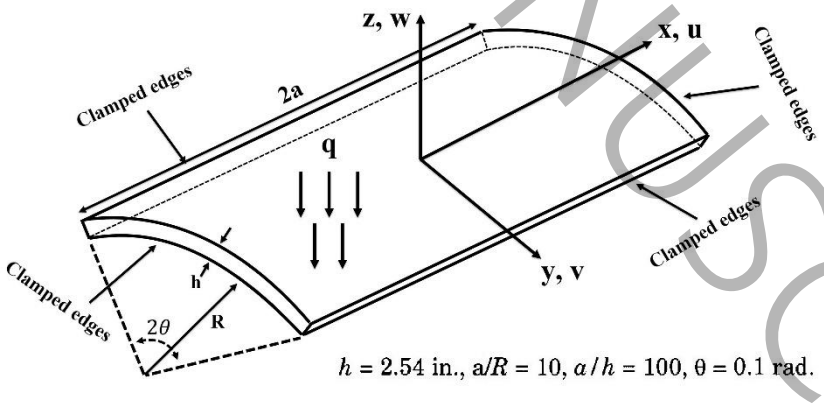

Fig. 11 Geometric characteristics of a clamped cross-ply (0/90) laminated cylindrical shell panel.

The material properties of the lamina are shown in Table 7 [48].

Table 7 Material properties of the lamina [48]

Property	Value
E_1 (psi)	25×10^6
$E_2 = E_3$ (psi)	10^6
$G_{12} = G_{13}$ (psi)	0.5×10^6
G_{23} (psi)	0.2×10^6
ν_{12}	0.25
ν_{23}	0.4

The center deflection of the laminated cylindrical shell panel under uniform load $q_0 = 1.2$ (psi) was computed for different numbers of elements and compared with the result reported by Reddy [48]; this comparison is presented in Table 8.

Table 8 Center deflection of the laminated cylindrical shell panel under uniform load

	w_0 (in)		
Number of elements	Present study	Reddy [48]	Error (%)
320	-0.52450	-	-
392	-0.63842	-	-
463	-0.66664	-	-
639	-0.67334	-	-
815	-0.67383	-	-
991	-0.67380	-0.67442	0.09 %

The convergence analysis was conducted for a laminated 2DTBC blade made of three layers of fiberglass epoxy with angles of 77.4, 43, and 43 degrees, [39]. For different element sizes, the backbone curve of the blade was obtained, as shown in Fig. 12. A total of 13,704 elements was selected as the optimal number for the nonlinear vibration analysis of the composite blade.

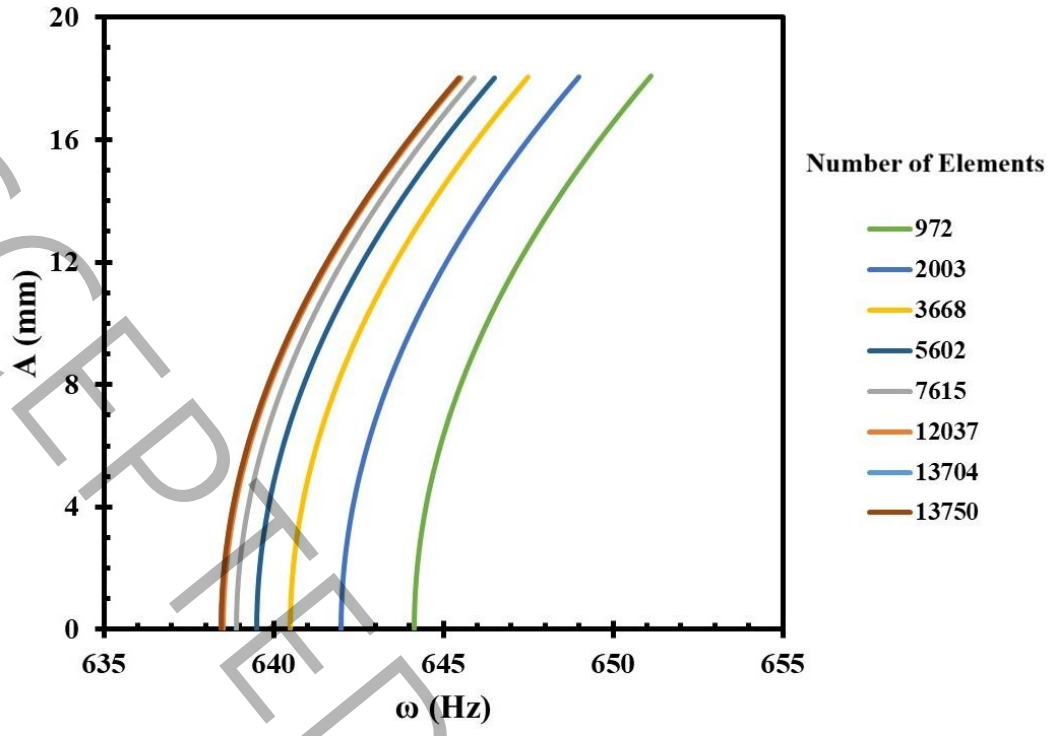

Fig. 12 Mesh convergence for backbone curves

To assess the precision of the backbone curve extraction method, the curve was computed for a square plate with supported boundary conditions and compared with the results that were obtained by Lewandowski [60]. The plate's dimensions and material properties are: side lengths a=b=0.401 m, thickness h=0.25 mm, elastic modulus E=206 GPa, density ρ=7700 Kg/m^3, and Poisson's ratio ν=0.3. Fig. 13 confirms that the obtained curve possesses the required precision and validity.

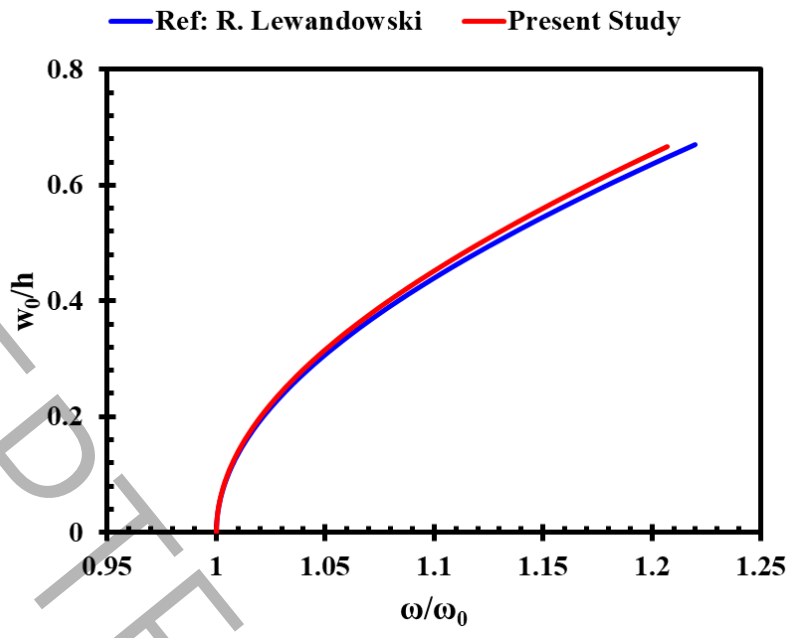

Fig. 13: The backbone curves for a square plate.

3-3- Optimization results

Leveraging the capabilities of MATLAB software, a single-objective genetic algorithm was used to optimize braided structure parameters to enhance hardening behavior. The results of this process are presented in Fig. 14 as two separate plots, with the horizontal axis representing the number of generations during the optimization process.

In Fig. 14(a), the vertical axis displays each generation's mean and best objective function values. The objective function is specified in Eq. (97). In Fig. 14(b), the vertical axis shows each generation's best, worst, and mean population scores. From the 60th generation onwards, the best score value remains unchanged, and this stability indicates the algorithm's convergence and the attainment of a stable optimal point.

The optimization process was repeated several times to ensure the achievement of a global optimum rather than just a local one. The plots presented in Fig. 14 are the result of the final and most successful

iteration of this optimization process, demonstrating the algorithm's convergence and success in achieving the desired objective.

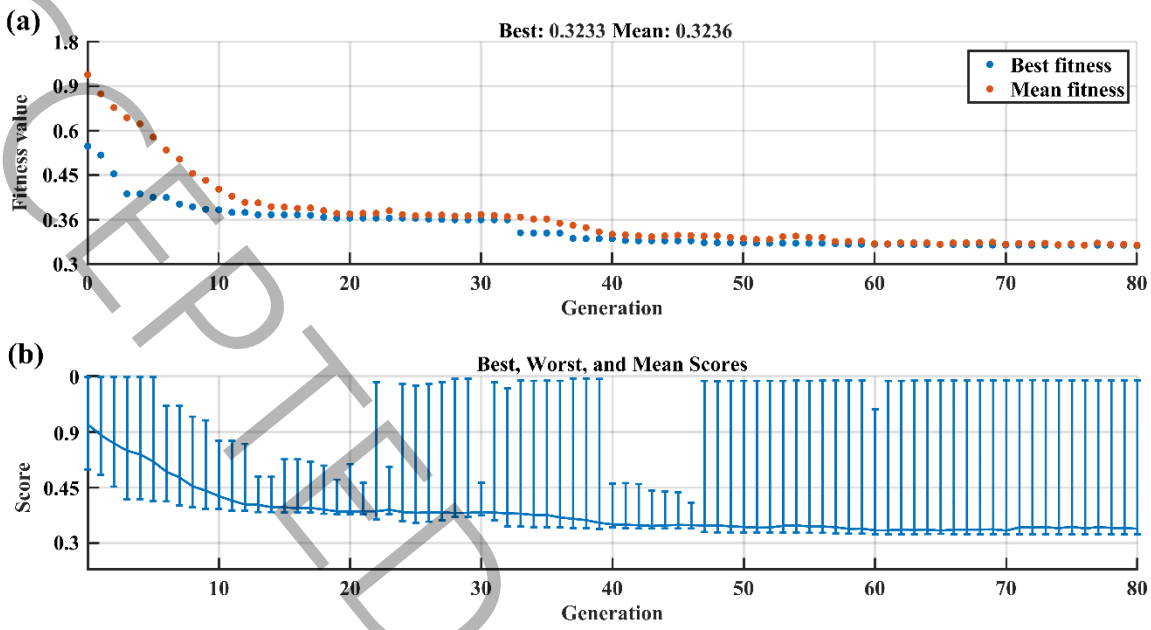

Fig. 14 Convergence trend of the genetic algorithm during optimization

Five of the 80 generations considered for the optimization process were randomly selected to examine the evolution of the optimal chromosomes throughout the process. The optimized values of the genes within these chromosomes, representing the braided structure parameters (such as braiding angle, braiding space, yarn count, and number of layers), are presented in Table 9. This table compares how the optimal values evolved across different generations, demonstrating how the genetic algorithm gradually converged towards better and more optimal solutions.

Table 9. Genetic algorithm's progression toward improved solutions

		Genes	Generation					
			1st	15th	30th	50th	70th	Optimum
	N	1	4	5	5	5	5	5
Layer 1	V_t	2	0.4166	0.1557	0.1541	0.1518	0.1476	0.1432
	V_c	3	0.5377	0.5776	0.5782	0.5907	0.593	0.5966
	C	4	0.48	0.4969	0.6534	0.6569	0.6737	0.6854
	D	5	0.543	0.7813	0.7911	0.7959	0.8032	0.8048
Layer 2	V_t	6	0.7735	0.5359	0.2883	0.2428	0.2313	0.2295
	V_c	7	0.4693	0.5154	0.5162	0.5567	0.5688	0.5695
	C	8	0.4994	0.5144	0.6591	0.6627	0.6642	0.7425
	D	9	0.5705	0.8408	0.8859	0.8906	0.9	0.9
Layer 3	V_t	10	0.4687	0.5062	0.5274	0.5294	0.5854	0.6009
	V_c	11	0.5267	0.6563	0.6704	0.7125	0.7127	0.8283
	C	12	0.4694	0.5879	0.6028	0.6181	0.7962	0.8289
	D	13	0.4652	0.7169	0.7403	0.8694	0.8888	0.8995
Layer 4	V_t	14	0.4964	0.4538	0.4363	0.4196	0.2944	0.178
	V_c	15	0.7755	0.553	0.3693	0.3209	0.2925	0.286
	C	16	0.4794	0.6359	0.6404	0.6406	0.6422	0.6665
	D	17	0.4977	0.7884	0.8138	0.8697	0.8828	0.8933
Layer 5	V_t	18	-	0.1832	0.1825	0.1801	0.1798	0.1782
	V_c	19	-	0.8143	0.8268	0.8381	0.8462	0.8462
	C	20	-	0.3028	0.2653	0.2466	0.2409	0.2403
	D	21	-	0.646	0.653	0.6618	0.6634	0.6694

Subsequently, the backbone curve of the transverse bending mode was plotted for each of the selected chromosomes, and the results were compared with the backbone curve corresponding to the final optimal point. Furthermore, the backbone curve corresponding to the optimized multilayer configuration obtained in the previous study [39] by maximizing the linear natural frequency is also included in Fig. 15 for comparison. The frequencies are presented in a dimensionless form to facilitate a more precise comparison between the natural frequencies associated with different chromosomes. The non-dimensionalization process $\left(\bar{\omega} = \omega / \omega_0\right)$ involves dividing a selected chromosome's natural frequencies $\left(\omega\right)$ by its first natural frequency $\left(\omega_0\right)$. This method shifts the analysis focus to the trend of frequency change in terms of displacement amplitude, rather than the absolute numerical values of the frequencies, thereby enabling a comparison of the performance of different chromosomes within a

uniform and comparable framework. A comparison of the curves indicates that the optimized curve exhibits a more pronounced hardening behavior than the others.

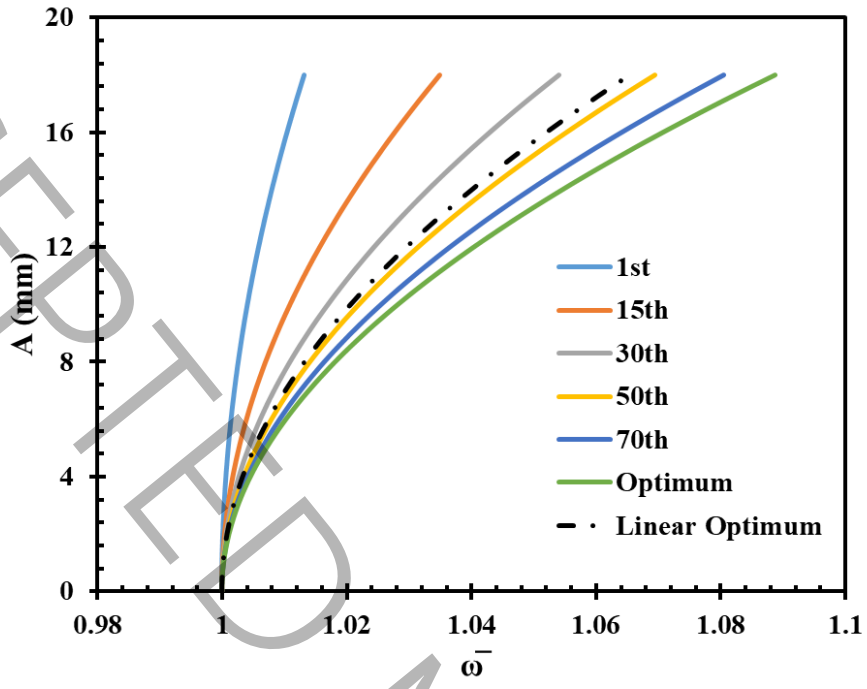

Fig. 15 Trend of increasing hardening behavior as shown by the backbone curves

To enable a quantitative evaluation of Fig. 15, the tangent line of amplitude with respect to $(\bar{\omega})$ (i.e., the slope of the backbone curve in a single point) has been computed for each design and is shown in Fig. 16. This slope provides a physically meaningful measure of the hardening behavior, as it reflects how rapidly the frequency increases with amplitude throughout the nonlinear regime. The results clearly demonstrate that the optimized structure exhibits a significantly lower slope than the initial design. This behavior is attributed to the increased structural stiffness and resistance to deformation of the structure.

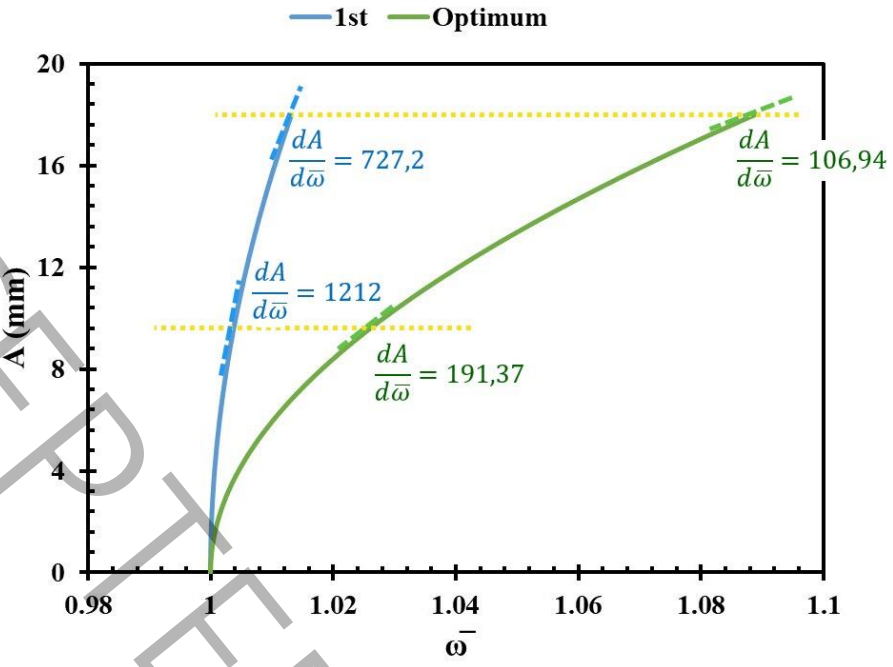

Fig. 16 Backbone curves slopes

Fig. 16 shows that the tangent slope of the optimized backbone curve at its endpoint is reduced by a factor of 727.2/106.94=6.8 compared to that of the non-optimized backbone curve (corresponding to the first generation). In other words, the hardening behavior of the structure in the optimized case is significantly enhanced.

A convergence assessment with respect to the number of harmonics was indeed conducted. When additional harmonic terms are included (e.g., $N_H = 3$), the slope of the backbone curve increases systematically at all amplitudes. Importantly, this increase is observed to be uniform across all designs and does not alter the relative trends between different configurations. As an illustrative example, a direct comparison between the two-harmonic $N_H = 2$ and three-harmonic $(N_H = 3)$ solutions for the first-generation design has been presented in the Fig. 17. Since the primary objective of this study is to enhance and compare hardening behavior across different designs rather than to predict absolute frequency values with maximum precision, retaining two harmonics provides a good balance between

computational efficiency and solution accuracy. Therefore, $(N_H = 2)$ is sufficient for the present optimization and does not affect the conclusions of the study.

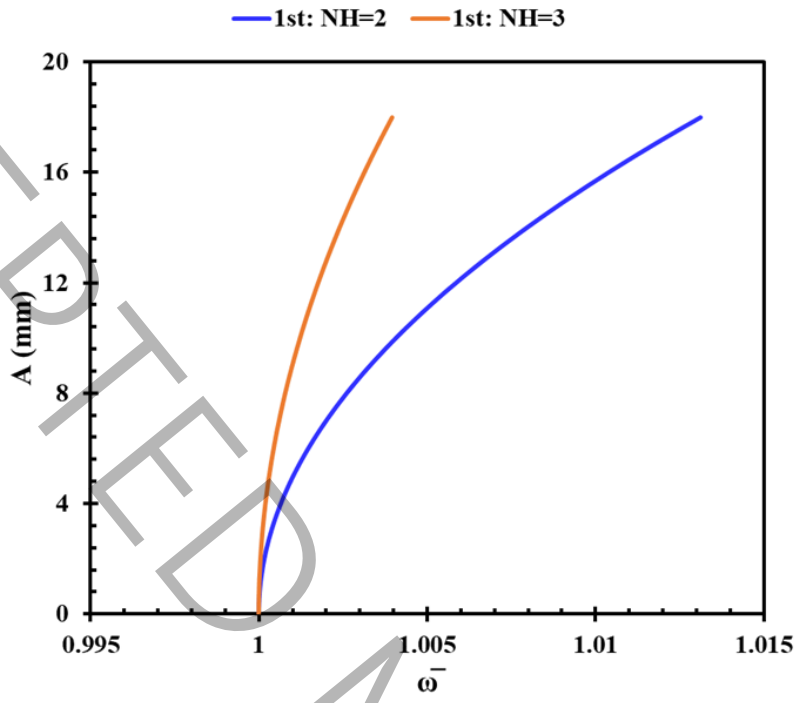

Fig. 17 A convergence assessment of the number of harmonics

Table 10 presents the optimized parameters of the braided structure for each layer of the composite, including braiding angle, braiding space, and yarn count, which had the most significant impact on increasing the blade's hardening behavior.

Table 10. Braiding parameters optimized using the genetic algorithm.

	Layer 1	Layer 2	Layer 3	Layer 4	Layer 5
Braiding angle (degree)	11	76	50	75	15
Yarn count (tex)	707	804	804	797	567
Braiding space (mm)	11.2	12	9.7	11.6	10.1

The mechanical behavior of triaxial braided composites is fundamentally different from that of conventional laminated composites such as unidirectional or woven laminates. Because of the intrinsic coupling between the axial and bias yarns, the influence of individual braiding angles cannot be

interpreted in isolation, and the resulting laminate behavior cannot be directly inferred using conventional stacking-sequence intuition. Therefore, the optimal layup reported in Table 10 is interpreted as the outcome of a global optimization process that exploits the complex coupling inherent in triaxial braided composites to tailor bending stiffness, bending–stretching, twisting-stretching, bending–twisting coupling, and geometric nonlinear behavior, rather than as a configuration that can be justified solely by conventional laminate theory rules.

4- Conclusion

This study aimed to enhance hardening behavior observable in the backbone curve of a 2DTBC blade, by optimizing the braided structure parameters. This was achieved by combining ANN modeling, analytical methods, finite element simulation, and single-objective genetic algorithm optimization. The following conclusions drawn.

- The integration of several distinct methods, including ANN, analytical methods, finite element simulation, and a single-objective genetic algorithm, provides a highly efficient and flexible approach for analyzing the nonlinear vibrational behavior of composite blades or other complex structures.
- It is possible to achieve a 2DTBC blade with optimized parameters that exhibit improved nonlinear vibrational performance compared to its initial state. In this study, by optimizing the structural parameters of the braid structure, an enhancement in the hardening behavior of the composite blade was achieved relative to its initial state. This aspect is crucial for composite fan blades that are subjected to large vibration amplitudes.
- The tangent slope of the optimized backbone curve at its endpoint is reduced by a factor of 6.8 compared to that of the non-optimized backbone curve. In other words, the hardening behavior of the structure in the optimized case is significantly enhanced.
- Due to its greater number of adjustable parameters compared to other conventional textile structures, the braided structure possesses a higher capacity for optimizing and enhancing the nonlinear vibrational behavior of composite structures, including fan blades.

5- Future work

- One of the key recommendations for investigating the nonlinear vibration behavior of composite blades is to consider the effect of rotation. Rotation increases the linear stiffness of the structure, induces additional membrane stresses, and increases the stress magnitude. When this stiffness combines with the nonlinear stiffness, it can have a significant impact on the nonlinear dynamic behavior and the shape of the backbone curve.
- It is recommended that the optimal braiding parameters be validated through experimental tests and nonlinear dynamic experiments, as this step represents the logical next phase for confirming the computational predictions.

Data availability

The corresponding author is willing to provide the datasets generated and used in this article to the applicant upon reasonable and justified request.

Funding

The Authors received NO FUNDING for this work.

References

[1] S.S. Rathore, V.R. Kar, Sanjay, Large-amplitude vibration of rotating functionally graded blades including geometrical nonlinearity and stress stiffening effects, Mechanics based design of structures and machines, 52(6) (2024) 3135-3159.
[2] D. Huang, W. Zhang, Y. Zhang, A. Amer, Nonlinear dynamics of graphene-reinforced aluminum matrix composite aero-engine blade in thermal environment, Composite Structures, 331 (2024) 117900.
[3] H. Guo, X. Ouyang, K.K. Żur, X. Wu, T. Yang, A.J. Ferreira, On the large-amplitude vibration of rotating pre-twisted graphene nanocomposite blades in a thermal environment, Composite Structures, 282 (2022) 115129.
[4] W. Zhang, X. Gu, Y. Zhang, New modeling on vibrations and bifurcations of FGGP reinforced pretwisted composite rotating blade under axial aerodynamic force: Theoretical and numerical researches, Thin-Walled Structures, 184 (2023) 110523.
[5] Y. Wang, J. Chen, Nonlinear free vibration of rotating functionally graded graphene platelets reinforced blades with variable cross-sections, Engineering Analysis with Boundary Elements, 144 (2022) 262-278.
[6] M. Amabili, Nonlinear vibrations of rectangular plates with different boundary conditions: theory and experiments, Computers & structures, 82(31-32) (2004) 2587-2605.
[7] M. Amabili, Do we need to satisfy natural boundary conditions in energy approach to nonlinear vibrations of rectangular plates?, Mechanical Systems and Signal Processing, 189 (2023) 110119.

[8] R. Gholami, R. Ansari, M.K. Hassanzadeh-Aghdam, S. Sahmani, Geometrically nonlinear higher-order shear deformable model of TiO2/GNP/polymer nanocomposite rectangular plates: A numerical study on mechanical properties and nonlinear primary resonance features, International Journal of Non-Linear Mechanics, (2025) 105209.
[9] H. Ovesy, P. Khaneh Masjedi, Investigation of the effects of constitutive equations on the free vibration behavior of single-celled thin-walled composite beams, Mechanics of Advanced Materials and Structures, 21(10) (2014) 836-852.
[10] G. Zuo, L. Hou, R. Lin, S. Ren, Y. Chen, Combination resonance and primary resonance characteristics of a dual-rotor system under the condition of the synchronous impact of the inter-shaft bearing, Scientific reports, 13(1) (2023) 1153.
[11] M.S. Taima, M.B. Shehab, T.A. El-Sayed, M.I. Friswell, Comparative study on free vibration analysis of rotating bi-directional functionally graded beams using multiple beam theories with uncertainty considerations, Scientific Reports, 13(1) (2023) 17917.
[12] W. Zhang, Structural design and dynamic characteristics analysis of braided composite two-stage gear transmission system, Scientific Reports, 14(1) (2024) 5584.
[13] M. Naghinejad, H.R. Ovesy, Free vibration characteristics of nanoscaled beams based on nonlocal integral elasticity theory, Journal of Vibration and Control, 24(17) (2018) 3974-3988.
[14] M. Naghinejad, H.R. Ovesy, Viscoelastic free vibration behavior of nano-scaled beams via finite element nonlocal integral elasticity approach, Journal of Vibration and Control, 25(2) (2019) 445-459.
[15] M. Naghinejad, H.R. Ovesy, Free vibration characteristics of nonlocal viscoelastic nano-scaled plates with rectangular cutout and surface effects, ZAMM-Journal of Applied Mathematics and Mechanics/Zeitschrift für Angewandte Mathematik und Mechanik, 101(5) (2021) e201900294.
[16] J. Yang, J. Xie, T. Wang, F. Yang, J. Chen, The vibration response mechanism of a blade disk rotor system under the coupling effects of cracks and aerodynamic forces, Scientific reports, 12(1) (2022) 1520.
[17] M. Yao, L. Ma, W. Zhang, Nonlinear Dynamics of the High-Speed Rotating Plate, International Journal of Aerospace Engineering, 2018(1) (2018) 5610915.
[18] N. Chandiramani, L. Librescu, C. Shete, On the free-vibration of rotating composite beams using a higher-order shear formulation, Aerospace Science and Technology, 6(8) (2002) 545-561.
[19] X. Gu, W. Zhang, Y. Zhang, A novel dynamic model on nonlinear vibrations of functionally graded graphene platelet reinforced rotating pretwisted composite blade considering subsonic airflow excitation and blade-casing rubbing, Composite Structures, 315 (2023) 116936.
[20] J. Chen, P. Cui, Q.-S. Li, Free vibrations of functionally graded graphene-reinforced composite blades with varying cross-sections, International Journal of Structural Stability and Dynamics, 20(14) (2020) 2043006.
[21] Y. Niu, M. Yao, Q. Wu, Resonance in dangerous mode and chaotic dynamics of a rotating pre-twisted graphene reinforced composite blade with variable thickness, Composite Structures, 288 (2022) 115422.
[22] Y.-J. Kee, S.-J. Shin, Structural dynamic modeling for rotating blades using three dimensional finite elements, Journal of Mechanical Science and Technology, 29 (2015) 1607-1618.
[23] K.K. Żur, J. Yuan, H. Guo, Z. Cheng, B. Bartoszewicz, On the vibration of hybrid turbine blades with an interaction between surface discontinuities and twist angle variation, Aerospace Science and Technology, (2025) 110035.
[24] S. Sina, H. Haddadpour, Axial–torsional vibrations of rotating pretwisted thin walled composite beams, International Journal of Mechanical Sciences, 80 (2014) 93-101.
[25] W. Zhang, G. Liu, B. Siriguleng, Saturation phenomena and nonlinear resonances of rotating pretwisted laminated composite blade under subsonic air flow excitation, Journal of Sound and Vibration, 478 (2020) 115353.
[26] M.M.H. Pour, H.R. Ovesy, Nonlinear dynamic buckling analysis of imperfect viscoelastic composite laminated plates, Struct. Eng. Mech, 79(5) (2021) 653-663.
[27] Z.-Z. Pan, X. Chen, L.-W. Zhang, Modeling large amplitude vibration of pretwisted hybrid composite blades containing CNTRC layers and matrix cracked FRC layers, Applied Mathematical Modelling, 83 (2020) 640-659.

[28] J. Poojary, V. Rajamohan, Nonlinear free vibration analysis of internal thickness-tapered multi-layered composite rectangular plates undergoing moderately large deflections, Journal of Sound and Vibration, 572 (2024) 118159.
[29] G. Liu, G. Chen, F. Cui, A. Xi, Nonlinear vibration analysis of composite blade with variable rotating speed using Chebyshev polynomials, European Journal of Mechanics-A/Solids, 82 (2020) 103976.
[30] Z.-M. Li, T. Liu, H. Kang, J. Tian, J. Jing, D. Wang, Theoretical and experimental investigations on steady-state responses of rotor-blade systems with varying rotating speeds based on a new nonlinear dynamic model, Mechanical Systems and Signal Processing, 184 (2023) 109692.
[31] E. Ansari, A. Setoodeh, T. Rabczuk, Isogeometric-stepwise vibrational behavior of rotating functionally graded blades with variable thickness at an arbitrary stagger angle subjected to thermal environment, Composite Structures, 244 (2020) 112281.
[32] X. Gu, Y. Zhang, W. Zhang, Q. Bi, Nonlinear analysis of a rotating pre-twisted composite blade reinforced with functionally graded graphene platelets under axial and transverse excitations, Nonlinear Dynamics, 111(14) (2023) 12947-12972.
[33] Y. Zhang, Y. Niu, W. Zhang, Nonlinear and chaotic vibrations of rotating functionally graded GPL reinforced composite pre-twisted blade subjected to aerodynamic force, Thin-Walled Structures, 181 (2022) 110135.
[34] X. Gu, W. Zhang, Y. Zhang, Nonlinear vibrations of rotating pretwisted composite blade reinforced by functionally graded graphene platelets under combined aerodynamic load and airflow in tip clearance, Nonlinear dynamics, 105(2) (2021) 1503-1532.
[35] P.-F. Dang, Z.-X. Yang, Y.-Y. Yan, Q.-K. Han, Z.-H. Jin, Nonlinear vibration characteristics of rotating composite blade considering the temperature-dependent graded material properties, Composite Structures, 258 (2021) 113419.
[36] M.-Y. Fan, J. Chen, Nonlinear dynamics of rotating functionally graded graphene platelets/titanium alloy trapezoid plates under 1: 3 internal resonance, Nonlinear Dynamics, 112(23) (2024) 20793-20812.
[37] H. Arvin, F. Bakhtiari-Nejad, Nonlinear free vibration analysis of rotating composite Timoshenko beams, Composite Structures, 96 (2013) 29-43.
[38] M.Y. Fan, J. Chen, Large amplitude vibration of rotating graphene reinforced titanium alloy dovetailed blades with general boundary conditions, Thin-Walled Structures, 208 (2025) 112801.
[39] M. Salehian, H.R. Ovesy, H. Dabiryan, Free vibration optimization of 2D tri-axial braided composite fan blade with ANN-Anal-FEM-GA integrated model, Scientific Reports, 14(1) (2024) 28819.
[40] Y. Niu, H. Ji, C. Tao, C. Zhang, Y. Wu, J. Qiu, Design of trailing edge flap based on MFC and prediction of deformation and aerodynamic performance using BP neural network, Journal of Intelligent Material Systems and Structures, (2025) 1045389X241305660.
[41] A.S. Azizi, M. Razbin, S.M. Mousavi, M. Li, A.A.R. Darzi, Enhancing thermal efficiency in twisted tri-lobe double pipe heat exchangers via integrated CFD and AI approaches, International Journal of Thermal Sciences, 206 (2024) 109331.
[42] A.A.R. Darzi, S.M. Mousavi, M. Razbin, M. Li, Utilizing neural networks and genetic algorithms in AI-assisted CFD for optimizing PCM-based thermal energy storage units with extended surfaces, Thermal Science and Engineering Progress, 54 (2024) 102795.
[43] S.M. Mousavi, A.S. Azizi, M. Razbin, A.A.R. Darzi, M. Li, Optimized design of helical-finned double pipe heat exchangers via numerical simulation and artificial intelligence, Applied Thermal Engineering, 258 (2025) 124605.
[44] M. Razbin, A.A. Gharehaghaji, M. Salehian, Y. Zhu, M.H. Kish, N.H. Kouchehbaghi, Artificial neural network-assisted theoretical model to predict the viscoelastic–plastic tensile behavior of polyamide-6 multi-ply yarns, Neural Computing and Applications, 36(29) (2024) 18107-18123.
[45] M. Razbin, M. Salehian, A.A. Gharehaghaji, A viscoelastic-plastic model for the core of various close-packings of multifilament polyamide-6 yarns, Scientific Reports, 14(1) (2024) 23800.
[46] F. Shahmoradi Ghaheh, M. Razbin, M. Tehrani, L. Zolfipour Aghdam Vayghan, M. Sadrjahani, Modeling and optimization of dyeing process of polyamide 6 and woolen fabrics with plum-tree leaves using artificial intelligence, Scientific Reports, 14(1) (2024) 15067.

[47] C. Zhang, W.K. Binienda, L.W. Kohlman, Analytical model and numerical analysis of the elastic behavior of triaxial braided composites, Journal of Aerospace Engineering, 27(3) (2014) 473-483.
[48] J.N. Reddy, Mechanics of laminated composite plates and shells: theory and analysis, CRC press, 2003.
[49] M.C. Da Silva, Non-linear flexural-flexural-torsional-extensional dynamics of beams—II. Response analysis, International Journal of Solids and Structures, 24(12) (1988) 1235-1242.
[50] M. Amabili, M.P. Paı¨ doussis, Review of studies on geometrically nonlinear vibrations and dynamics of circular cylindrical shells and panels, with and without fluid-structure interaction, Appl. Mech. Rev., 56(4) (2003) 349-381.
[51] A. Saood, A.H. Khan, M.I. Equbal, K.K. Saxena, C. Prakash, N.I. Vatin, S. Dixit, Influence of fiber angle on steady-state response of laminated composite rectangular plates, Materials, 15(16) (2022) 5559.
[52] X. Liu, Backbone Curve Analysis of Nonlinear Mechanical Systems, University of Sheffield, 2018.
[53] T. Detroux, L. Renson, L. Masset, G. Kerschen, The harmonic balance method for bifurcation analysis of large-scale nonlinear mechanical systems, Computer Methods in Applied Mechanics and Engineering, 296 (2015) 18-38.
[54] K. Worden, Nonlinearity in structural dynamics: detection, identification and modelling, CRC Press, 2019.
[55] P. Ribeiro, M. Petyt, Non-linear free vibration of isotropic plates with internal resonance, International journal of non-linear mechanics, 35(2) (2000) 263-278.
[56] R.E. Mickens, Truly nonlinear oscillations: harmonic balance, parameter expansions, iteration, and averaging methods, World Scientific, 2010.
[57] C. VanDamme, M. Allen, A. Madrid, Using the harmonic balance method to directly compute NNMs of geometrically nonlinear finite element models, in: Proceedings of the International Conference on Noise and Vibration Engineering (ISMA), Leuven, Belgium, 2018.
[58] M. Petyt, P. Ribeiro, Geometrical non-linear periodic vibration of plates, in: ASME International Mechanical Engineering Congress and Exposition, American Society of Mechanical Engineers, 2000, pp. 61-72.
[59] P. Ribeiro, M. Petyt, Nonlinear vibration of plates by the hierarchical finite element and continuation methods, International Journal of Mechanical Sciences, 41(4-5) (1999) 437-459.
[60] R. Lewandowski, On beams membranes and plates vibration backbone curves in cases of internal resonance, Meccanica, 31(3) (1996) 323-346.